IOWA STATE UNIVERSITY
Digital Repository

2012

Wave scattering by an integral stiffener

Ricky Steven Reusser
Iowa State University

Follow this and additional works at: https://lib.dr.iastate.edu/etd

Part of the Engineering Mechanics Commons

Wave scattering by an integral stiffener

by

Ricky Steven Reusser

A thesis submitted to the graduate faculty

in partial fulfillment of the requirements for the degree of

MASTER OF SCIENCE

Major: Engineering Mechanics

Program of Study Committee:

Stephen D. Holland, Major Professor

Dale E. Chimenti

Ron A. Roberts

Thomas J. Rudolphi

Iowa State University

Ames, Iowa

2012

TABLE OF CONTENTS

LIST OF FIGURES

ACKNOWLEDGEMENTS

First and most importantly, I would like to thank my advisor, Dr. Steve Holland, for his unending guidance and support in my graduate education. He has helped me through many difficult and challenging times even when I asked more of him than I should have. I would also like to thank committee members Dr. Dale Chimenti, Dr. Ron Roberts, and Dr. Thomas Rudolphi for their guidance and support in my graduate and undergraduate education. A large portion of this work is the result of many informative talks about guided waves with Dr. Roberts and I thank Dr. Chimenti profusely both for his mentoring and patience.

ABSTRACT

Integral stiffeners act as a frequency dependent filter for guided plate waves, impeding transmission and limiting the performance of ultrasonic structural health monitoring (SHM) systems. The effect of integral stiffeners on an acoustic leak location system for manned spacecraft is examined. Leaking air is turbulent and generates noise that can be detected by a contact-coupled acoustic array to perform source location and find the air leak. Transmission of guided waves past individual stiffeners is measured across a frequency range of 50 to 400 kHz for both high and low aspect-ratio rectangular stiffeners. Transmission past a low aspect ratio stiffener is correlated with the ability to locate leaks in the presence of multiple stiffeners. A simple explanatory model that illuminates the underlying mechanics of waves crossing a stiffener is developed using impedance methods. Good agreement is seen with numerical calculations using the boundary element method and with the experimental measurements. The model aids the designer and indicates transmission and reflection are determined by longitudinal and flexural stiffener resonances. It is demonstrated that operating in frequency ranges of high plate wave stiffener transmission significantly improves the reliability of noise source location in the spacecraft leak location system. A protocol is presented to enable the selection of an optimal frequency range for leak location.

CHAPTER 1.   Introduction

Stiffeners represent one of the fundamental structures underlying many engineering structures. They are often the most efficient way to add flexural rigidity with minimal material. Most stiffeners are bonded or welded to a plate-like surface, but where high performance is required, integral stiffeners may be preferable. Although the geometry is nearly identical, the integral stiffeners under consideration in this work are composed of rectangular strips of material machined rather than bonded to the larger structure.

This work considers the effects of integral stiffeners in the context of structural health monitoring (SHM) non-destructive evaluation (NDE) systems. The specific application considered in the first part of this work is an ultrasonic leak location system for spacecraft structures. The system uses phased array sensors to passively detect leak-generated noise transmitted through the plate-like pressure vessel as guided waves. Integral stiffeners machined into the pressure vessel scatter the leak-generated noise and limit the range of the array detectors.

The first part of this work examines the behavior of the detection system in the presence of integral stiffeners and uses the transmission characteristics of the stiffeners to suggest an algorithm for determining the optimal frequency range at which the leak detection system should operate.

The second part of this work looks more closely at normal incidence of guided waves upon a stiffener. An explanatory model is developed and indicates that the scattering is a result of both flexural and longitudinal resonances in the stiffener.

CHAPTER 2.   Guided plate wave scattering at vertical stiffeners and its effect on source location

R. S. Reusser, D. E. Chimenti, R. A. Roberts, S. D. Holland

Center for Nondestructive Evaluation

and Aerospace Engineering Department

Iowa State University

Ames IA 50011 USA

2.1   Abstract

This paper examines guided wave transmission characteristics of plate stiffeners and their influence on the performance of acoustic noise source location. The motivation for this work is the detection of air leaks in manned spacecraft. The leaking air is turbulent and generates noise that can be detected by a contact-coupled acoustic array to perform source location and find the air leak. Transmission characteristics of individual integral stiffeners are measured across a frequency range of 50 to 400 kHz for both high and low aspect-ratio rectangular stiffeners, and comparisons are made to model predictions which display generally good agreement. It is demonstrated that operating in frequency ranges of high plate wave stiffener transmission significantly improves the reliability of noise source location in the plate. A protocol is presented to enable the selection of an optimal frequency range for leak location.

2.2   Introduction

Stiffeners are used in aerospace structures to add structural rigidity with minimal additional weight. *In situ* structural health monitoring (SHM) non-destructive evaluation (NDE) systems use ultrasonic guided waves to evaluate structural integrity (1). The interaction of guided waves with structural features limits the range of ultrasonic SHM sensors. Typical NDE and SHM applications use piezoelectric actuators to excite guided wave modes in the kilohertz to low-megahertz range. The waves propagate through the structure, and after interacting with a feature of interest, they propagate to a detector. Analysis of the detected waveforms gives information on structural degradation. Thus, the interaction of guided waves with lap joints (2; 3), stringers (6), more complex joints (13), or integral stiffeners controls the amount of energy that eventually reaches the detector.

This paper considers the influence of rectangular stiffeners typical in spacecraft structures on guided plate wave propagation. This type of integral stiffener is machined directly into the structure in order to add flexural rigidity with minimal weight. Many studies have considered the similar problems of guided wave reflection from rectangular notches (6; 2; 7; 8), step thickness changes (9), or strip weldments (10). Wilcox et al. analyze an adhesively bonded stringer using the Semi-Analytical Finite Element method and observe variation in guided wave transmission as the incident angle of waves upon the straight feature is varied (6). We show here, based on experimental data and Boundary Element Method (BEM) simulations (4), that rectangular stiffening ribs act like a geometric filter, producing some frequency bands with high transmission across stiffeners, and other frequency bands with low transmission. This filtering behavior limits performance of an SHM systems such as ours that locates leaks in manned

spacecraft.

2.2.1 Spacecraft Leak Location

Manned spacecraft are at risk of orbital debris and micrometiorite impact (12; 13) which can generate an air leak. Because of the limited oxygen on board, it is imperative to quickly locate a leak. Turbulence-generated airborne noise is the conventional method of locating leaks in pressure vessels. In space, because the air leaks into the vacuum, the leak noise flows outward with the air and there is almost no airborne noise generated inside the spacecraft. In addition, equipment and life support systems mounted against the pressure vessel wall inhibit access and preclude rapid location of an air leak. The method we have reported (14) relies instead on ultrasonic noise (20-400 kHz) generated by the leak in the skin of the spacecraft structure, through aerodynamic coupling of the escaping air to the plate-like pressure vessel wall. An acoustic array provides directional information on the arriving noise signals. Temporal correlations extract the statistics of the noise signal arriving at one array element compared to signals from all the other elements of the array (15). Because the signals are random and continuous, the signal acquisition and processing can proceed sequentially, significantly reducing the expense of the electronics. Extension of the two-dimensional spatio-temporal analysis of Alleyne and Cawley (16) to three dimension transforms the measured correlations into frequency-wavevector space. The direction of the wavevector under the sensor array indicates the direction to the noise signal source. Triangulation with two or more arrays locates the leak.

Successful leak location has been demonstrated on simulated spacecraft structure using a 64-element diced PZT (lead zirconate titanate) piezoelectric array detector (17). Our own prior work (14; 18) has shown that integral stiffeners may limit performance of the leak location pro-

cedure. In an environment where prompt and accurate leak location is critical, the system and procedure must be robust, so the current work focuses on a study of guided wave propagation in spacecraft structures to evaluate stiffener transmission characteristics, and uses those results to develop a frequency selection protocol for optimal detection center frequency and bandwidth.

We find that guided wave transmission measurements performed at normal incidence using a piezoelectric point source and an ideal optical virtual array receiver are consistent with BEM simulations over a frequency range of 50 to 400 kHz for two types of stiffener geometry. Since the transmission varies greatly with frequency, and the location of the passbands (transmitted frequencies) are strongly geometry-dependent, it is best to include the entire frequency range in the active analysis. When integrated over the entire detection spectrum, the passbands dominate the other frequencies, producing accurate results.

2.3 Transmission across a Stiffener

The theory of guided Lamb waves is well known (9). Geometric obstructions, such as the integral stiffeners considered here, scatter guided Lamb modes, resulting in reflection and transmission as well as mode conversion of an incoming wave. The reflection and transmission depend on frequency, aspect ratio, guided wave mode, and incident angle. The stiffener acts as a geometry-dependent filter of the guided wave; It is observed that certain frequency bands have high transmission and other frequency bands have high reflection (5). Transmission across the stiffener seems to be related to resonances which, in the case of non-normal incidence, map to feature-guided waves that propagate along the stiffener (6).

2.3.1 Theory

A single guided mode incident upon a stiffener may be mode-converted into multiple scattered modes. The overall behavior is represented with an energy transmission coefficient, defined at frequency ω by

$$T(\omega) = \frac{\sum_n E_n^{\text{tr}}(\omega)}{\sum_n E_n^{\text{inc}}(\omega)}, \tag{2.1}$$

where E_n^{tr} and E_n^{inc} are the transmitted and incident energies of the nth guided wave modes, respectively. Because the A_0 and S_0 modes are the only propagating modes that exist at low frequency, and because the A_0 mode dominates over the symmetric mode under the asymmetric excitation used in our experiments, only the A_0 mode need be considered. With that simplification, the transmission coefficient is

$$T(\omega) \approx \frac{E_{A_0}^{\text{tr}}(\omega)}{E_{A_0}^{\text{inc}}(\omega)}. \tag{2.2}$$

Observing that energy is proportional to the square of amplitude, the expression can further be simplified to

$$T(\omega) = \frac{|A_{A_0}^{\text{tr}}(\omega)|^2}{|A_{A_0}^{\text{inc}}(\omega)|^2}. \tag{2.3}$$

2.3.2 Experiment

To measure transmission of the lowest order antisymmetric, or A_0, Lamb mode across an integral stiffener, a laser vibrometer measures modal amplitudes of incident and transmitted guided waves created by a piezoelectric contact transducer. The methodology is similar to that of Morvan et al. (11) to study Lamb wave reflection from the free edge of a plate, and has been used extensively for SHM applications (22; 23; 24). Because the guided wave amplitude will be a superposition of incident and reflected waves as well as waves reflected from the boundaries,

amplitudes are sampled along a line containing the source and perpendicular to the stiffener, as depicted in Fig. 2.1. The cross denotes the location of the contact source transducer, and two independent 1-dimensional coordinate scans with the laser vibrometer (indicated by the lines of dots) measure the incident and transmitted waves. Because the signal is repeatable only a single point need be measured at a time for the wavefield to be reconstructed. Data is captured until all ringing and wave propagation have decayed to below the noise threshold.
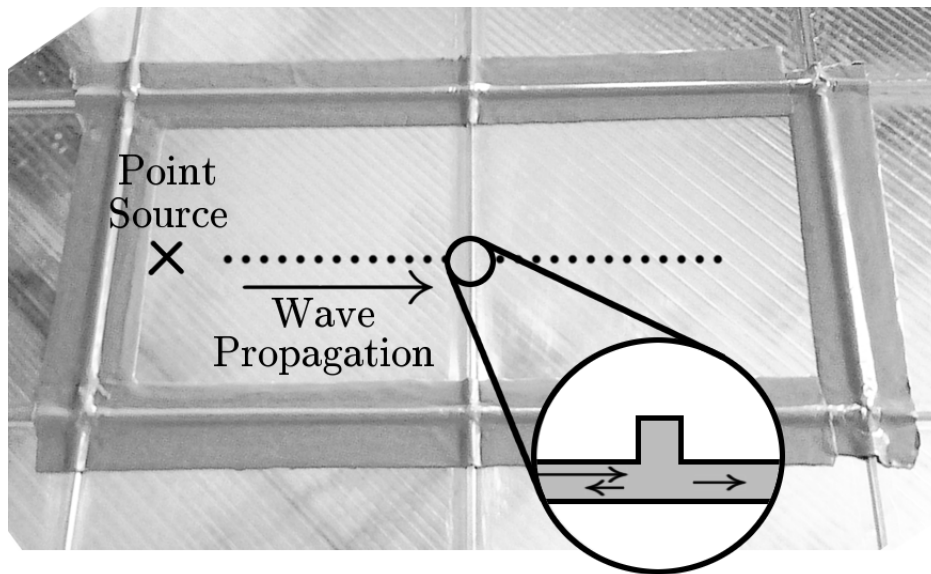
Figure 2.1   Photo of 6×6-foot sample showing experimental area isolated by butyl rubber (seen as a low-reflection band on the perimeter). Source is marked with a cross, and two sets of dots show the locations of laser vibrometer linear virtual-array measurements of incident and scattered guided wave fields. Inset shows stiffener cross-section with arrows representing waves incident upon as well as transmitted and reflected by stiffener.

Two aluminum samples have been studied in these experiments. The first has a thickness of 3.175 mm (1/8 inch) with stiffeners having a square cross section of 4.76×4.76 mm machined directly into the plate, so there is no material boundary between the plate and the stiffener. The second plate has a thickness of 3.175 mm with stiffeners 2.54 mm wide and 22 mm in height. To isolate the response of a single stiffener, sound-absorbing putty is layered around

the perimeter of the experimental area so that reflections are almost completely suppressed, even at the lowest frequency of 50 kHz. A representation of the experimental geometry is shown in the inset of Fig. 2.1. The incident, reflected, and transmitted waves are shown for the short, or low aspect-ratio, stiffener.

A 9.5-mm diameter contact transducer with a non-resonant ultrasonic horn that reduces the contact area to roughly 1 mm^2 induces guided waves in the plates. A Panametrics pulser/receiver excites the transducer, which is fixed to the specimen with couplant and light pressure for the duration of the test. Because of asymmetric single-side excitation, most of the energy resides in the A$_0$ Lamb mode.

At each point in the scan, a Polytec OFV-5000/OFV-505 Laser Vibrometer measures the out-of-plane particle velocity of the plate surface. At the frequencies involved, the sensitivity of the laser vibrometer is very poor compared piezoelectric sensors. The point contact horn on the source transducer best approximates a point source, but is inefficient. Because of these conditions, 10^4 averaged impulse responses at a simulated leak source acquired at a rate of 100 Hz, provide the desired signal-to-noise ratio. To achieve the best results, the full usable spans of the plates are scanned with 1 mm spacing.

To correct for radial falloff of the waves as they spread in two dimensions, the signal measurements are normalized by $1/\sqrt{r}$, where r is the distance from the noise source to the measurement location. A spatio-temporal Fourier transform of the measured signal (16; 25), permits separation of the modes and guided wave propagation directions in frequency-wavenumber space. A spatial Kaiser window applied before the Fourier transform reduces sidelobes. Finally, amplitudes are sampled along the incident and transmitted A$_0$ mode curves, and the transmission coefficient is calculated per frequency with Eq. (3.42).
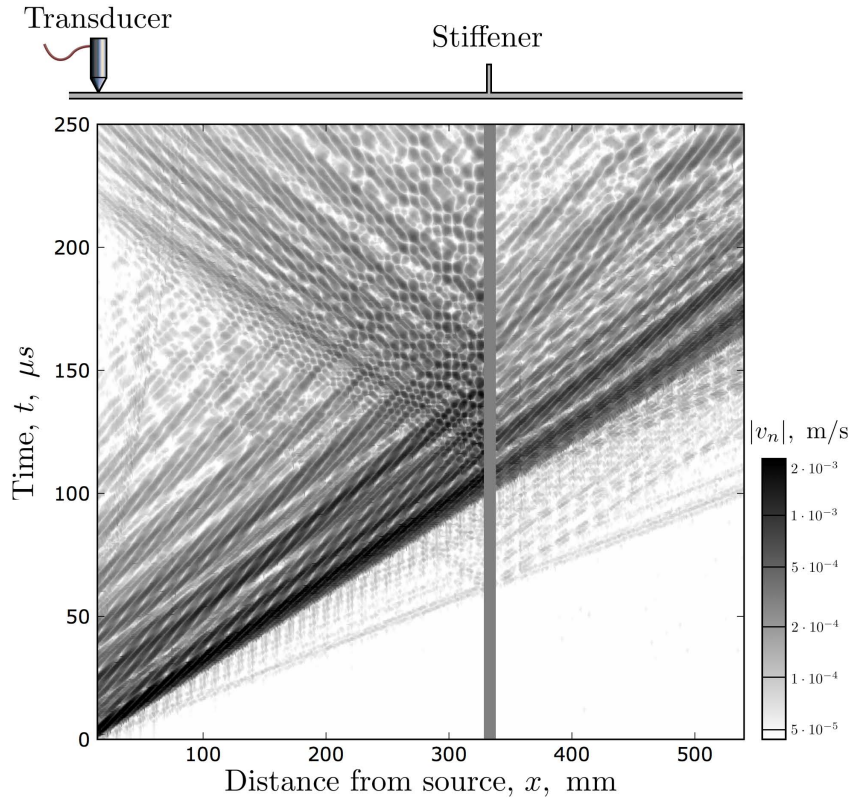
Figure 2.2   Measured normal component of particle velocity magnitude displayed as a gray-scale plot in coordinate x and time t for the tall stiffener test section. The wave amplitude is represented by the surface particle velocity v_n

Figure 2.2 illustrates a portion of the measured $x - t$ diagram for scattering from the tall stiffener. The magnitude of the normal component of the velocity magnitude is plotted in a logarithmic gray-scale (higher amplitude, darker value) in time from $t = 0$ to $t = 250\mu$s and in space from the source at $x = 0$ to the stiffener at $x = 325$ mm and beyond out to 550 mm from the source, both segments acquired with 1 mm spacing.   Visible in the data are the incident S_0 and A_0 modes. Although the A_0 mode has greater out of plane velocity than the S_0 mode for a given energy flux, the incident energy flux of the S_0 mode is still only ten percent that of the A_0 mode at the center frequency (200 kHz). A portion of the incident S_0 energy mode converts to A_0. When the stronger but slower incident A_0 waves meet the stiffener, there is significant
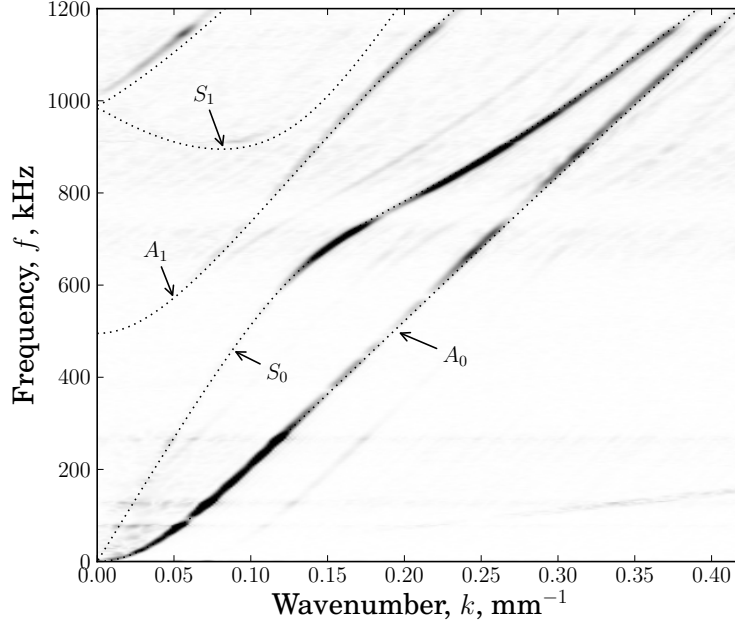
Figure 2.3   Measured dispersion curves for incident guided plate waves in the high aspect-ratio test section. Calculate Lamb wave dispersion curves (dotted lines) are superimposed.

reflection and transmission of energy with little conversion. A very close examination shows that a small amount of $A_0 \rightarrow S_0$ mode conversion does occur in the transmitted waves, but it amounts to only 5% of the incident energy flux.

Interestingly, on the left side of the figure the vibrometer detects a very faint, and very slow, acoustic wave which appears as a faint line from the source to about 80 mm at $t = 250\mu$s. The wave speed matches the 340 m/s speed an acoustic wave travels in air.

The measured incident wave spectrum, the 2-D Fourier transform of the data of Fig. 2.2, is shown in Fig. 2.3.   The data fall onto discrete mode curves which coincide with normal modes of the plate, $i.e.$, Lamb waves. The spectrum of the source transducer together with the amount of out-of-plane moton for a given mode and frequency determines the magnitude at each point on the dispersion curves. Higher normal wave motion leads to a larger detected

amplitude, such as between 100 and 300 kHz and 0.05 to 0.15 mm^{-1} in the wavenumber for the A_0 mode. Between 600 and 900 kHz the lowest order symmetric mode S_0 is also rather strongly excited, but very little of the S_0 mode is seen below 500 kHz.

2.3.3 Comparison of Experiment with BEM Simulation

Computational modeling of the stiffener transmission frequency dependence is corroborated through comparison to these experimental measurements. The models of stiffener transmission were previously developed and reported (4; 5). The computational model employed to generate the predictions of transmission behavior presented here is based on the Boundary Element Method (BEM). This particular formulation starts with a boundary integral equation formulation of the scattering problem, using principles of elastodynamic reciprocity between the sought wave field and the elastodynamic response to an applied point load (Green function) (3). The formulation separates the problem geometry into two semi-infinite plates attached to a joining body. It is assumed in formulating the problem that neither the geometry of the stiffened plate nor the incident plate wave field has a spatial dependence on the direction parallel to the length of the stiffener, thereby reducing the formulation to a 2D scattering problem. By virtue of reciprocity principles, the computation requires only explicit determination of wave field displacements and tractions on the surface of the joining body, via the numerical solution of a governing boundary integral equation. Transmission and reflection coefficients are extracted by employing fields computed on the joining body surfaces to which the semi-infinite plates attach in an associated reciprocity relation expressing the response of a semi-infinite plate to applied edge fields. Established integral equation solution methods are employed, which project boundary fields onto discrete basis functions, thereby transforming the boundary integral equation

into an algebraic matrix equation, variously referred to as the Method of Moments (MoM), or the Boundary Element Method (BEM) (27; 2). A more detailed exposition of the computational model used to generate the results presented here is found in (4). Others methods have been applied to plate wave transmission at a geometric disruption, such as application of Finite Element Analysis (6). The benefit of a semi-analytical approach such as the one used here is that the semi-infinite plates can be modeled explicitly.

Application of the computational model to the stiffened plate defines the joining body to consist of the stiffening rib plus the adjacent section of the plate to which the stiffening rib is integrally attached (see Figure 2.1). The surface of the joining body is sub-divided into adjacent boundary segments, over each of which the sought wave field is represented as a quadratic polynomial. Employing this field representation in the governing boundary integral equation yields a matrix equation for the polynomial coefficients. For the low aspect ratio stiffener (4.76 × 4.76 mm), 5 boundary segments were prescribed on each face of the stiffener, and on each plate attachment surface, yielding a total of 30 segments. Three polynomial coefficients for the 2D wave field on each segment results in a 180 × 180 coefficient matrix, the inversion of which yields the desired field on the plate attachment surfaces. The width and height of the high aspect ratio stiffener (2.54 × 22 mm) was subdivided into 2 and 15 segments, respectively, with 5 segments prescribed over the plate attachment surfaces, leading to inversion of a 264 × 264 coefficient matrix. Applying the computed plate attachment wave field to the edge of the semi-infinite plate and employing field reciprocity as described in (5) yields computed versions of the guided wave transmission coefficients referred to in Eq. (3.42).

Fig. 2.4 shows measured and simulated transmission coefficients of a high aspect ratio stiffener. The measured coefficient is calculated from data in Fig. 2.2 to evaluate Eq. (3.42)
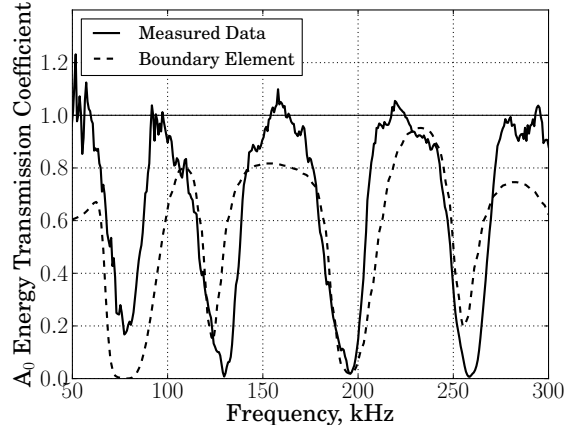
Figure 2.4   Experimental and theoretical energy transmission coefficients across the tall aspect-ratio stiffener, with the incident guided wave at normal incidence to the stiffener. The theoretical curve is the result of the boundary element method calculation.

using the procedure described above. The measured and simulated coefficients share a periodic structure with with a period of roughly 70 kHz and minima around 120, 190 and 250 kHz. This confirms the passband/stopband nature of the stiffeners when interacting with guided waves. Despite a high sensitivity of the exact stopband frequencies to geometry and elastic properties, the stopband frequencies match to within about 5 kHz. The small portion of S_0 not accounted for in Eq. (3.42) allows the transmission coefficient to slightly exceed 1.0 at some frequencies.

Similarly, Fig. 2.5 shows the measured and simulated energy transmission coefficient of the A_0 mode in the low aspect-ratio stiffener. The general shape of the two curves is similar. Both start at a transmission coefficient of 1.0 in the low frequency regime and have relative minima at approximately 100 and 260 kHz. The transmission coefficient increases to approximately 1.0 above 300 kHz. The analysis neglects mode conversion of incident A_0 energy into transmitted S_0, which is again on the order of 5%. As for the high aspect ratio stiffener, the small percentage of transmitted A_0 energy originating from S_0 due to the asymmetric geometry allows the transmission coefficient to appear to slightly exceed 1.0.
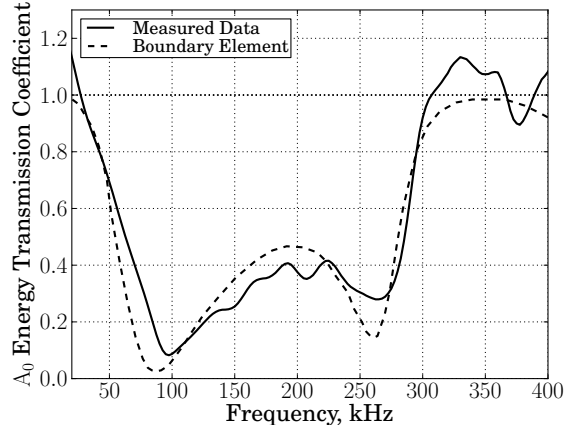
Figure 2.5   Experimental and theoretical energy transmission coefficients across the low aspect ratio stiffener, with the incident guided wave at normal incidence to the stiffener. The theoretical curve is the result of the boundary element method calculation.

The narrow stop bands observed in Fig. 2.4 for the high aspect ratio stiffener are the signature of a resonance. Transmission is blocked when the phase of the incident wave and the phase of a reflection in the stiffener come into alignment. For the low aspect ratio stiffener, we hypothesize that such a resonance is less well defined, hence the broader relative bandwidth of the stopband. If true, this would be very important for all structural health monitoring applications because a sufficiently wide stopband could block most of the ultrasonic signal bandwidth when crossing a stiffener.

2.4   Spacecraft Leak Location

We now consider the performance of a spacecraft leak location system (14; 18) in the presence of integral stiffeners. Because the diameter of the spacecraft is much larger than the longest ultrasonic wavelength, the vessel wall can be accurately modeled as the same sort of flat plate used in evaluating the effect of stiffeners (29).

2.4.1 Theory

To summarize the guided wave source location method briefly, the signal generated by the source and arriving at the jth element of the detector array can be expressed, for distance $|\mathrm{x}_j| \gg 1/k_n(\omega)$, as

$$v(\mathrm{x}_j, \omega) = N(\omega)|\mathrm{x}_j|^{-1/2} \sum_n A_n(\omega) \exp(i\, k_n(\omega)|\mathrm{x}_j|), \tag{2.4}$$

where v represents the normal particle velocity at the jth array element at position x_j and frequency ω to be measured with the laser vibrometer. The term N represents the complex amplitude and phase of the source, and the propagating waves are summed over all guided wave modes n with amplitude coefficient A_n. We can represent the jth array element vector position x_j as the sum of the array reference position x_0 and a relative element position s_j,

$$\mathrm{x}_j = \mathrm{x}_0 + \mathrm{s}_j. \tag{2.5}$$

The distance to a specific element can be written using the far-field approximation as

$$|\mathrm{x}_j| = |\mathrm{x}_0| + \mathrm{d} \cdot \mathrm{s}_j, \tag{2.6}$$

where d is a unit vector representing the direction of wave propagation under the array. Then, substitution into Eq. 2.4 yields

$$v(\mathrm{x}_j, \omega) = N(\omega)|\mathrm{x}_0|^{-1/2} \sum_n A_n(\omega) \exp\left[i\, k_n(\omega)(|\mathrm{x}_0| + \mathrm{d} \cdot \mathrm{s}_j)\right]. \tag{2.7}$$

The detector array (PZT or laser vibrometer) is not infinitely large, so its finite spatial extent means that a spatial window function $W(\mathrm{x})$ is applied to the acquired data. The two-dimensional Fourier transform of Eq. 2.7 in transform variables k and ω gives

$$\mathrm{FT}\left\{W(\mathrm{x})v(\mathrm{x}, \omega)\right\} = \sum_n B_n \widehat{W}(\mathrm{k} - k_n\mathrm{d}), \tag{2.8}$$

where $\widehat{W}$ is the Fourier-transformed window function and the amplitude coefficients have been grouped into B_n which is implicitly dependent on frequency. Representing the data in a two-dimensional wavenumber map, the energy in all modes n and at frequency ω lies along a line emanating from the origin and in the dominant direction of wave propagation d. This direction can then be discerned by inspection of the map. Summing over a particular frequency range $\Delta\omega$ enhances the detectability of the leak. This operation results in a much improved detection accuracy and a more robust leak location method. Suppressing the parametric dependence on frequency ω and local array vector s, we have

$$\sum_{\omega_1}^{\omega_2} \mathrm{FT}\{W\,v\} = \sum_{\omega_1}^{\omega_2} \sum_{n} B_n\,\widehat{W}(\mathrm{k} - k_n \mathrm{d})\,. \tag{2.9}$$

That is to say, the 3-D spatio-temporal $(x,\,y,\,t)$ Fourier transform of the measured detector array data, summed over the relevant frequency band, gives a map of the propagating waves under the array in terms of $\mathbf{k} = (k_x, k_y)$, blurred by the limited spatial sensing range and windowing. The above analysis makes no assumptions about the wave source. The noise from the leak (our desired "signal") is in fact random, but we cross correlate it, which makes it deterministic. In most ultrasonic experiments, we time gate our detection to eliminate the interference from late arrivals. With the correlated random source, this is not possible. In the experiments below we have done sufficient averageing that the "noise" we are fighting comes not from the detector but instead from interference from alternate wave paths.

2.4.2   An Algorithm for Selecting a Frequency Band

Selection of the proper frequency band is critical to determining the most probable leak location and minimizing the number of required sensors. Three factors determine this frequency band: leak noise spectrum, array detector sensitivity, and noise transmission across structural

features. A robust leak location system must operate in the intersection of these three criteria.

Basic turbulence theory predicts the leak energy coupled into the plate will decrease with frequency (30), and in fact it is observed that no usable leak noise lies beyond roughly 400 kHz. This finding matches the sensitivity of the detector, which operates up to 500 kHz. Thus the useful noise for spacecraft leak location is noise below 400 kHz which is minimally scattered by the spacecraft structure.

The most straightforward algorithm for locating the high transmission frequencies, termed *in situ* calibration, collocates a simulated leak with each detector array. The calibration is determined by sensing the simulated leak signal from each of the other non-collocated detector arrays. Location of one simulated leak at a time with each of the other sensors determines the calibration. The disadvantage of this method is that it requires additional complexity, power, and cost of additional source transducers. to act as simulated leaks. The second method, termed *wide-bandwidth* analysis, simply uses the full functional range of the array detector. By integrating over all available frequencies that may provide a correct answer, those frequencies that transmit through stiffeners tend to dominate the measured signals.

2.4.3   Experimental Configuration

A 6×6 foot plate containing a 1 foot grid of low aspect-ratio stiffeners simulates a section of a spacecraft pressure vessel. (A small section of the same plate was used for the low aspect-ratio stiffener transmission measurement in Section 2.) Forty-three different simulated leak locations have been arbitrarily distributed across the surface of the plate. The point contact transducer is excited with a Panametrics pulser/receiver in a manner identical to the stiffener transmission tests.

The laser vibrometer virtual array consists of a 12×12 scanned point array on a 27.5×27.5 mm area with 2.5 mm spacing between the optical beam points. The out-of-plane motion is captured with the laser vibrometer using 200 triggers per point, averaged. Waveforms at each point are acquired sequentially and the direction of wave propagation is determined from Eq. 2.9. Fewer averages are needed here than the 10^4 needed for the stiffener transmission measurement because the very high signal-to-noise ratio is not required and because the measured response can be integrated over frequency. Throughout the tests, the optical array location is not moved. Instead, the piezoelectric source transducer is attached to the plate with mild pressure and a very thin layer of butyl rubber for acoustic coupling and is moved to simulate different leak locations relative to the stiffener.

The results of one of the simulated *in situ* calibration tests are plotted in Fig. 2.6. The spatial Fourier transform is zero-padded to 128×128 points in the x and y directions and uses a rectangular window. Each data point in the plot has been integrated with a 25-kHz bandwidth from 75 to 100 kHz. After summing, the data is integrated along a set of radial lines with $0.5°$ resolution. The angle with the largest integral is selected and plotted at each source point with a solid line. Each "x" in the figure corresponds to a simulated leak location, and the single circle shows the location on the 6×6-foot plate of the scanned laser vibrometer array. The arrows at each "x" correspond to the most likely direction of the arriving wave vector, as measured at the open circle. The arrow lengths have been scaled for ease of interpetation so they nearly reach the detector. The diagonal dashed lines represent the low aspect-ratio integral stiffeners. Figure 2.6 shows the results of all 43 tests with the wavenumber map integrated over a frequency range extending from 75 to 100 kHz, as described in (14). For each test, only the strongest observed wavevector has been sampled and plotted. Although some of the simulated
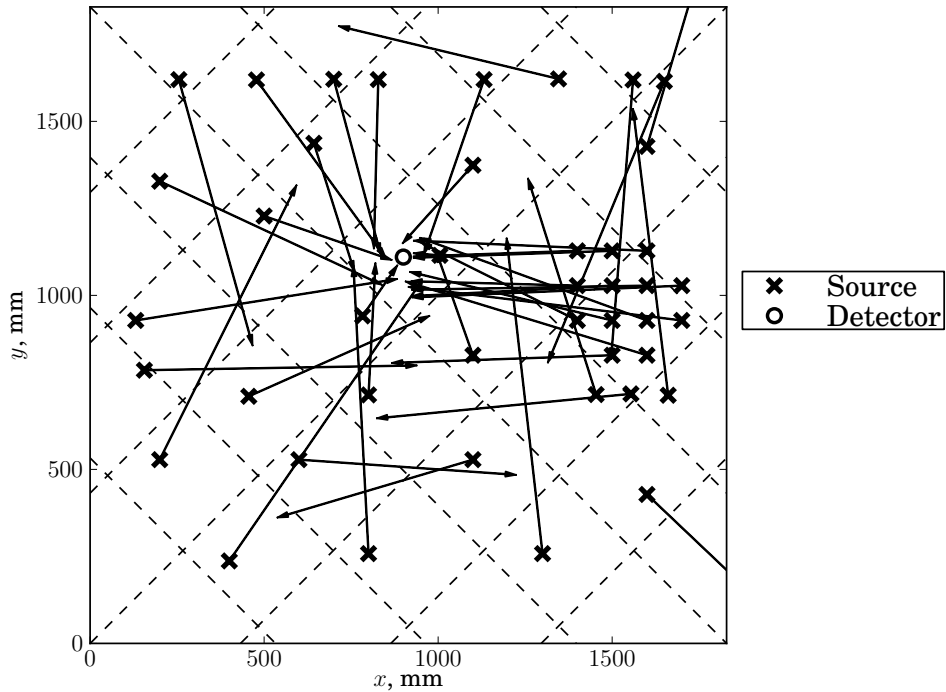
Figure 2.6   Leak location results for frequencies from 75-100 kHz. The "×" markings show simulated leak locations, and the circle near the plate center shows the detector array position. The diagonal dashed lines are the locations of the integral stiffeners.

leaks are correctly located by the laser vibrometer array in Fig. 2.6, the performance is generally quite poor when the 75-100 kHz frequency range is used. Many of the arrows are not pointing even approximately toward the location of the array.

Contrast this behavior with the measurements of the same test analyzed in a frequency range from 375-400 kHz, as shown in Fig. 2.7.   In this figure, essentially none of the prediction measurements, even across as many as four stiffeners, is in error by more than 5° for the range 375–400 kHz. Because there are no coupling variations, as when using a physical PZT array detector, and because the ratio of signal to detector noise was very high, the behavior observed here must be entirely caused by coherent interference of alternate wave paths from the source to detector array.
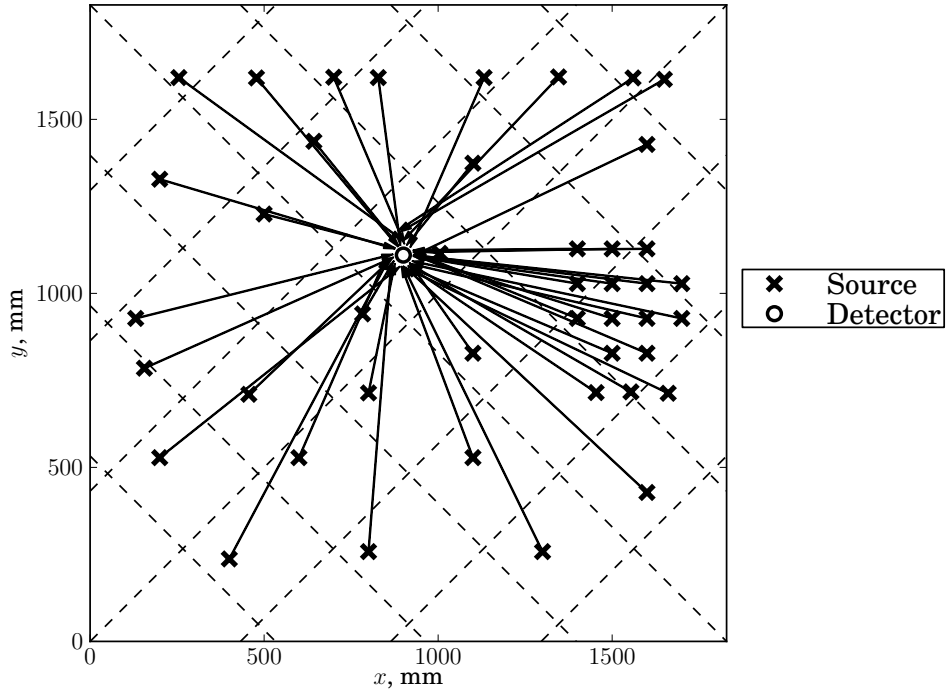
Figure 2.7   Leak location results for frequencies in the range 375–400 kHz. The "×" markings show simulated leak locations, and the circle shows the detector array position. The diagonal dashed lines are the integral stiffeners. The arrows, indicating the predicted source directions based on the measured data, are now essentially all correct.

These observations using the laser vibrometer detector match very closely the measured performance of the PZT array detector, when it is also operated in this frequency range. Furthermore, these results are completely consistent with the stiffener transmission coefficients in Fig. 2.5. In tests with either the laser vibrometer or PZT array, leak location occurs with consistent accuracy mainly above 275 kHz. Although the test data shown in Fig. 2.7 indicate clearly that the guided wavevectors are not always normal to the stiffener, as they are in the transmission coefficients plotted in Fig. 2.5, the data of Fig. 2.7 strongly suggest that normal-incidence transmission still is a good indicator of leak location performance.

The strong correlation described above between stiffener transmission and accurate leak
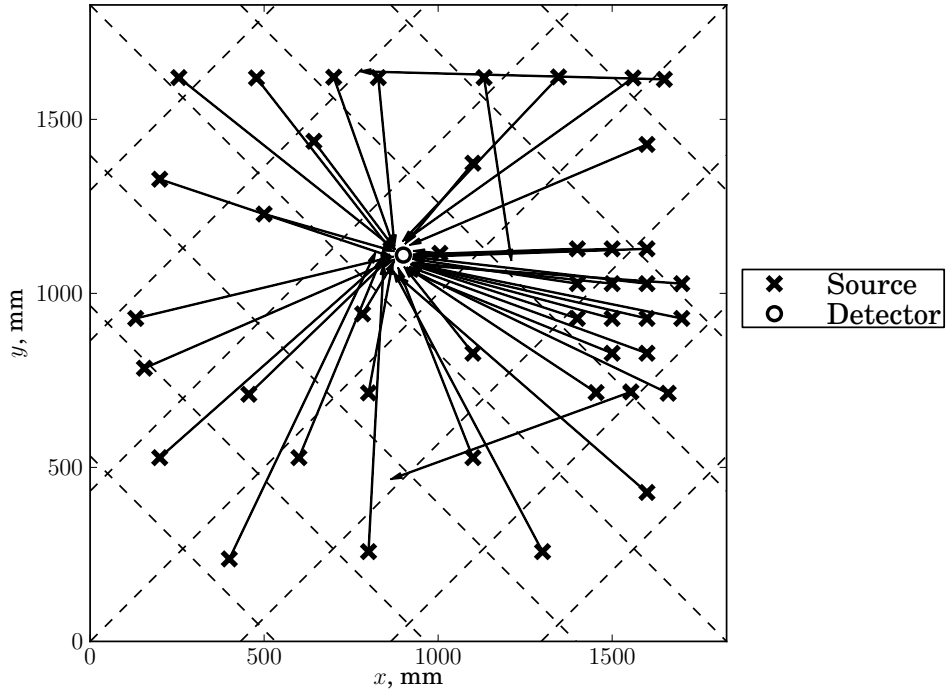
Figure 2.8   Normalized leak location maps for frequencies in the range 100–475 kHz. The "×" markings show simulated leak locations, and the circle shows the detector array position. The diagonal dashed lines are the integral stiffeners. The arrows, indicating the predicted source directions based on the measured data, are still nearly all correct, as they were in Fig. 2.7.

location seems to favor *in situ* calibration as the preferable algorithm for frequency range selection. Not all stiffener geometries, however, have such wide passbands and stopbands. For the tall stiffener (2.54 mm wide by 22 mm high) Fig. 2.4 shows the measured and calculated transmission coefficients, but with much narrower passbands and stopbands. Moreover at non-normal incidence the frequencies can scale or shift, which could lead to an absence of any frequency bands with consistently good transmission.

In fact, there is no real need to choose such a narrow frequency band. Figure 2.8 shows data from the same tests   as those presented in Figs. 2.6–2.7, but with the maps normalized so as to weight all frequencies equally when integrated from 100 to 475 kHz. Normalization

prevents a single spurious frequency from dominating the entire result. This *wide-bandwidth* algorithm demonstrates accurate leak location for 40 of the 43 tests. Although this result does not quite match the nearly perfect performance of Fig. 2.7, it does demonstrate that a simpler, more robust strategy can still locate leaks with high accuracy. For a practical array, which will not have flat frequency response, the response could similarly be normalized, within the constraints of detector noise. To compensate for that dependence, which can include coupling variations and wave damping, we would need to reformulate the protocol to give extra weight to those frequency ranges where the signal is stronger owing to these extrinsic effects.

2.5   Summary and conclusions

Measurements and simulations have shown that integral stiffeners pass ultrasonic waves in some frequency bands while almost entirely blocking them in others. High aspect ratio stiffeners seem to block transmission at their resonance. BEM simulations accurately predict this stopband/passband behavior, despite the sensitivity of the stopband and passband frequencies to stiffener height and elastic properties. As a result of these stopbands and their variation in frequency with incident angle, it will be best to take advantage of all available frequencies in finding the direction to the leak source. Further investigations might include the examination of the angular dependence of guided wave transmission and mode conversion at off-normal incidence on an integrally stiffened plate.

Bibliography

[1] A. Raghavan, C. E. S. Cesnik, "Review of Guided-wave Structural Health Monitoring," *The Shock and Vibration Digest* **39**(2), pp. 91-114, (2007).

[2] M. J. S. Lowe, R. E. Challis, C. W. Chan, "The transmission of Lamb waves across adhesively bonded lap joints," *J. Acoust. Soc. Am.* **107**(3), pp. 1333-1345, (2000).

[3] E. Lindgren, K. Jata, B. Scholes, J. Knopp, "Ultrasonic plate waves for fatigue crack detection in multi-layered metallic structures," *Proc. SPIE* 6532, 653207 (2007).

[6] P. Wilcox, A. Velichko, B. Drinkwater, A. Croxford, "Scattering of plane guided waves obliquely incident on a straight feature with uniform cross-section," *J. Acoust. Soc. Am.* **128**(5), pp. 2715-2725, (2010).

[13] D. W. Greve, N. Tyson, I. J. Oppenheim, "Interaction of defects with Lamb waves in complex geometries," *IEEE Ultrasonics Conference Proceedings*, 297-300, (2005).

[6] B. A. Auld, M. Tan, "Symmetrical Lamb Wave Scattering at a Symmetrical Pair of Thin Slots," *Ultrasonics Symposium*, pp. 61-66, (1977).

[7] F. Benmeddour, S. Grondel, J. Assaad, Emmanuel Moulin, "Study of the fundamental Lamb modes interaction with symmetrical notches," *NDT & E International* **41**, pp. 1-9, (2008).

[8] A. Demma, P. Cawley, M. J. S. Lowe, "Scattering of the fundamental shear horizontal mode from steps and notches in plates," *J. Acoust. Soc. Am.*, **113**(4), pp. 1880-1891, (2003).

[9] Y. Cho, "Estimation of ultrasonic guided wave mode conversion in a plate with thickness variation," *IEEE Transactions on Ultrasonoics, Ferroelectrics, and Frequency Control* **47**(3), pp. 591-603, (2000).

[10] Y. N. Al-Nasser, S. K. Datta, A. H. Shah, "Scattering of Lamb waves by a normal rectangular strip weldment," Ultrasonics, **29**(2), pp. 125-132, (1991).

[4] R. A. Roberts, "Guided wave propagation in integrally stiffened plates," in *Review of Progress in Quantitative Nondestructive Evaluation*, vol. 27, D. O. Thompson, D. E. Chimenti, Eds. (AIP Press, New York, 2008), pp. 170–177.

[12] D. S. F. Portree and J. P. Loftus, Jr, "Orbital debris: A chronology," NASA Technical Paper *TP-1999-208856*, (1999).

[13] D. J. Kessler, "Sources of orbital debris and the projected environment for future spacecraft," J. Spacecraft **18**, pp. 357-360, (1981).

[14] S. D. Holland, D. E. Chimenti, R. A. Roberts, and M. Strei, "Locating air leaks in manned spacecraft using structure-borne noise," *J. Acoust. Soc. Am.* **121**, pp. 3484–3492 (2007).

[15] S. M. Ziola, M. R. Gorman, "Source location in thin plates using cross-correlation," *J. Acoust. Soc. Am.* **90**(5), pp. 2551-2556, (1991).

[16] D. Alleyne, P. Cawley, "A two-dimensional Fourier transform method for the measurement of propagating multimode signals," *J. Acoust. Soc. Am*, **89**(3), pp. 1159-1168, (1991).

[17] S. D. Holland, R. A. Roberts, D. E. Chimenti, Jun-Ho Song, "An ultrasonic array sensor for spacecraft leak direction finding," Ultrasonics **45**, pp. 121–126 (2006).

[18] S. D. Holland, R. A. Roberts, D. E. Chimenti, and M. Strei, "Leak detection in spacecraft using structure-borne noise with distributed sensors," Appl. Phys. Lett. **86**, 174105-1–3 (2005).

[9] J. D. Achenbach, *Wave propagation in elastic solids,* American Elselvier, (1973).

[5] R. A. Roberts, "Plate wave transmission/reflection at geometric obstructions: model study," *Review of Progress in Quantitative Nondestructive Evaluation*, vol. 29, D. O. Thompson, D. E. Chimenti, Eds. (AIP Press, New York, 2010), pp. 192–199.

[11] B. Morvan, N. Wilie-Chancellier, H. Duflo, A. Tinel, J. Duclos, "Lamb wave reflection at the free edge of a plate" in J. Acoust. Soc. Am. **113**(3), pp. 1417-1425, (2003).

[22] W. J. Staszewski, B. C. Lee, L. Mallet, F. Scarpa, "Structural health monitoring using scanning laser vibrometry: I. Lamb wave sensing," *Smart Mater. and Struct.*, **13**, pp. 251-260, (2004).

[23] L. Mallet, B. C. Lee, W. J. Staszewski, F. Scarpa, "Structural health monitoring using scanning laser vibrometry: II. Lamb waves for damage detection," *Smart Mater. Struct.*, **13**, pp. 261-269, (2004).

[24] W. H. Leong, W. J. Staszewski, B. C. Lee, F. Scarpa, "Structural health monitoring using scanning laser vibrometry: III. Lamb waves for fatigue crack detection," *Smart Mater. Struct.*, **14**, pp. 1387-1395, (2005).

[25] D. H. Johnson, *Array Signal Processing: Concepts and Techniques*, Prentice Hall, 1993.

[3] J. D. Achenbach, *Reciprocity in Elastodynamics*, (Cambridge Univ Press, London, 2003).

[27] W. C. Gibson, *The Method of Moments in Electromagnetics.* Chapman & Hall, CRC Press, 2008.

[2] A. Cheng, D. Cheng, "Heritage and early history of the boundary element method," *Engineering Analysis with Boundary Elements* **29**, pp. 268-302, (2005).

[29] D. C. Gazis, "Three-Dimensional Investigation of the Propagation of Waves in Hollow Circular Cylinders. II. Numerical Results" *J. Acoust. Soc. Am.* **31**(5), pp. 573-578, (1959).

[30] S. B. Pope, *Turbulent Flows*, (Cambridge University Press, London, 2000).

CHAPTER 3.   Reflection and transmission of guided plate waves by vertical stiffeners

R. S. Reusser, D. E. Chimenti, R. A. Roberts, S. D. Holland

Center for Nondestructive Evaluation

and Aerospace Engineering Department

Iowa State University

Ames IA 50011 USA

3.1   Abstract

The interaction of guided plate waves with integral stiffeners limits the spatial range of structural health monitoring non-destructive evaluation systems. This paper develops a simple explanatory model that illuminates the underlying mechanics of waves crossing a stiffener. The model aids the designer and indicates transmission and reflection are determined by longitudinal and flexural stiffener resonances. Good agreement is seen with numerical calculations using the boundary element method and with experimental measurements.

3.2   Introduction

Stiffeners add flexural rigidity and buckling resistance to aerospace structures while minimizing weight. Many structural health monitoring (SHM) non-destructive evaluation (NDE) concepts rely on the ability of ultrasonic guided waves to propagate a long distance from actuator to defect to detector in order to monitor structural integrity with a minimum of sensors (1). Integral stiffeners interfere with propagating ultrasonic waves, limiting the effective range. SHM sensors typically operate in kilohertz to low-megahertz range. Since useful wavelengths are typically similar in length scale to the stiffeners, scattering is a complicated process that results in a pattern of stopbands and passbands. Based on our observations and calculations, guided wave transmission past an integral stiffener is determined by the pattern of resonances within the stiffener.

Figure 3.1 shows the geometry for wave scattering by an integral stiffener. Incoming wavefronts parallel to the stiffener enter from the left. Upon interacting with the stiffener, a portion of the waves are reflected back to the left, and the remaing energy is transmitted in waves that exit to the right. Points representing the center of the junction (point J), the base of the stiffener (point B), and the end of the stiffener (point E) are marked on the diagram.

Since scattering problems quickly becomes complex for non-trivial geometries, a great deal of effort has been expended developing approximate and numerical solution techniques. The most mathematically complete technique for linear elastic wave equations is the boundary element method (BEM) (2) Using the Reciprocity theorem (3), the problem is reduced to an integral discretized along the boundary of the geometry (4) (5). More recent developments expand on the well-known finite element method (FEM) to improve the spectral properties of
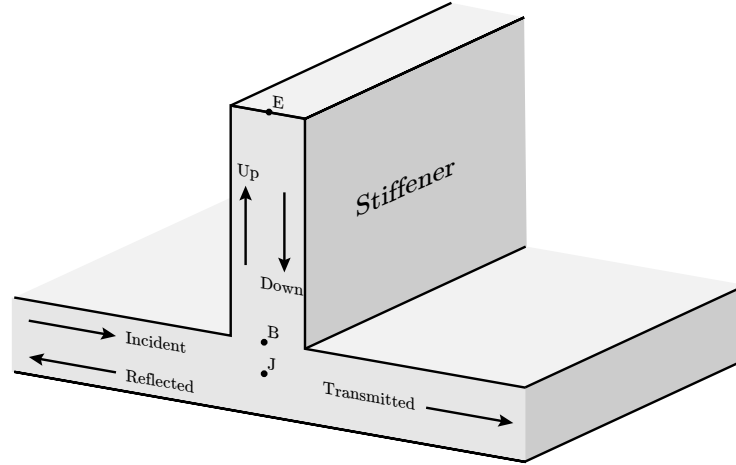
Figure 3.1   Coordinate system for the stiffener cross-section, SHM transducer on the left transmitting to an SHM receiver on the right.

solutions when dealing with propagating waves. These techniques are used very successfully to analyze wave interaction with similar geometries (6). However, the downside of such numerical techniques is that the complexity obscures the fundamental mechanics governing the problem.

Analytical approximations have been developed, but primarily for the cases of waves in rods and rod impact. Lee and Kolsky (7) consider stress waves in circular rods as they pass pass through an angular junction. By matching displacements and rotations at the joint, they develop a theory that couples the two rods together and reproduces the experimentally observed transmission and reflection of flexural and longitudinal waves. Yong and Atkins (8) also consider transient wave propagation in square rods forming a T-junction, modeling the junction as a rigid cube. Using Timoshenko beam theory, they observe good agreement with experiments as longitudinal waves in the terminating rod approach a T-junction, pass through the joint, and spread outward symmetrically. In a similar manner, we use the theory of guided waves in plates to develop an approximate model for wave transmission past a stiffener. Through a straightforward approximation and impedance techniques from transmission line theory, the

transmission coefficient is observed to be near unity at resonance (low stiffener mechanical impedance) and near zero between resonances (high stiffener mechanical impedance.)

3.3   Approximate Model

3.3.1   High aspect ratio approxmation

The primary approximation in our model is that the aspect ratio of the stiffener is large (much taller than it is thick). In this situation, the stiffener itself behaves as another plate. Guided waves travel up and down it, interacting with the junction at one end and the free surface at the other. The stiffener functions as a finite plate coupled to the larger plate. Similarly, at some distance away from the stiffener, the waves traveling in the plate must approach guided Lamb modes, for which an explicit solution and various approximations are well known (9). The same holds in the stiffener away from either the junction or the free end. Thus, the problem of guided wave scattering by a high aspect ratio stiffener is governed by the interaction of guided Lamb modes with the junction and free end of the stiffener.

3.3.2   Small junction approximation

A number of exact solution techniques exist for Lamb wave reflection from the free edge of a plate. Y. Cho combines a boundary element method with the normal mode expansion technique (10), and Morvan *et al.* apply stress-free conditions at a number of colocation points along the free edge (11). No such technique exists for the more complicated junction between plate and stiffener. Typical approaches utilize numerical discretization, using either the Boundary Element Method (BEM) (5) Finite Element Method (FEM) (12; 13), or, more recently, the Semi-Analytical Finite Element (SAFE) method (6). These techniques are consistent, meaning

they approach the exact mathematical solution as grid resolution or discretization order are increased, but at the cost of a great deal of computation. When the junction region is small relative to wavelength of the guided plate waves, the precise mechanics of the junction become less significant. As a result, the sections that meet at the junction may be though of as directly coupled in displacement and rotation.

3.3.3 Low frequency approximation

The result of these approximations is that at low frequencies, the problem may be solved through the combination of Lamb wave solutions with matching conditions where they meet. This assumption leads to an approximate solution that still accurately captures the fundamental mechanics of the scattering problem.

At low frequencies where translation and rotation of the stiffener cross section are more significant than distortion, there are three primary degrees of freedom and corresponding forces at each point along the plate. The state of the plate at a given point is defined by displacements

$$\mathbf{u} = \begin{bmatrix} u \\ v \\ \theta \end{bmatrix}, \tag{3.1}$$

where u is horizontal particle displacement, v is vertical displacement, and θ is counterclockwise cross section rotation, and forces

$$\mathbf{F} = \begin{bmatrix} H \\ V \\ M \end{bmatrix}, \tag{3.2}$$

where H is horizontal force per depth averaged across the cross-section, V is vertical force per depth, and M is the moment per depth acting on the cross section.

3.3.4 Generalized Impedance

Forces in a linear dynamic system may be related to the resulting particle velocities through a mechanical impedance, typically defined as

$$F = Z\dot{u}, \tag{3.3}$$

where F is force, Z is impedance (in N/(m/s)), and $\dot{u}$ is the time derivative of displacement u. Impedance representation simplifies analysis, making the resulting transmission and reflection coefficients relatively simple functions of impedance. This approach is commonly used in the study of electronic transmission lines (14) where voltage and current are used in place of force and particle velocity, respectively. Unlike electronic transmission lines when there is a single force (voltage) and proportional degree of freedom (current), mechanical plates have three forces (normal, shear, and moment) and three mechanical degrees of freedom (horizontal velocity, vertical velocity, and rotational velocity). We can define a generalized impedance matrix $\mathbf{Z}$ that relates the three forces to the three velocities,

$$\mathbf{F} = \mathbf{Z}\dot{\mathbf{u}}, \tag{3.4}$$

where the bold symbols $\mathbf{F}$ and $\dot{\mathbf{u}}$ indicate vectors of length 3, and $\mathbf{Z}$ is an 3×3 impedance matrix coupling each degree of freedom to each of the forces. Writing out all components explicitly,

$$\begin{bmatrix} H \\ V \\ M \end{bmatrix} = \begin{bmatrix} z_{11} & z_{12} & z_{13} \\ z_{21} & z_{22} & z_{23} \\ z_{31} & z_{32} & z_{33} \end{bmatrix} \begin{bmatrix} \dot{u} \\ \dot{v} \\ \dot{\theta} \end{bmatrix}. \tag{3.5}$$

3.3.5 Junction

The free body diagram in Fig. 3.2 cuts the problem into three plates that meet at junction J. The stiffener has a free end at point E. The subscript I/R indicates forces resulting from
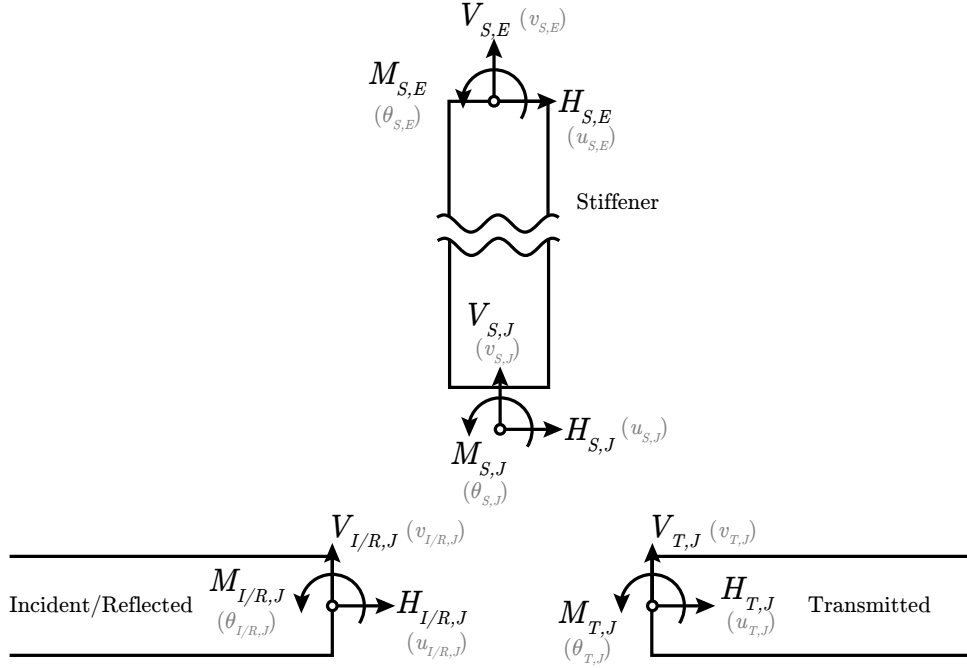
Figure 3.2   Free body diagram of the stiffener cross-section with corresponding displacements in parentheses.

the superposition of incident and reflected waves, the subscript T indicates forces resulting from transmitted waves, and the subscript S indicates forces resulting from the superposition of waves traveling up and down the stiffener. All forces illustrated on the diagram indicate complex amplitudes of time-harmonic forces at the cross section centers. These forces are averaged across the cross section so that a single force at the cross-section center represents the force applied to the whole cross-section.

Using these definitions, a guided wave of frequency f traveling in an unbounded plate may be said to have a characteristic generalized impedance $\mathbf{Z}_0$ that fixes the relationship between $\mathbf{F}$ and $\dot{\mathbf{u}}$ for all types of waves the plate permits,

$$\mathbf{F} = \mathbf{Z}_0\dot{\mathbf{u}}. \tag{3.6}$$

3.3.6 Force Balance

If the three plates in Fig. 3.2 meet at a junction with no volume, then forces must balance according to Newton's 2nd Law, leading to the system of equations

$$\begin{cases} \sum H = 0 : & H_{I/R,J} + H_{T,J} + H_{S,J} = 0 \\ \sum V = 0 : & V_{I/R,J} + V_{T,J} + V_{S,J} = 0 \\ \curvearrowleft \sum M = 0 : & M_{I/R,J} + M_{T,J} + M_{S,J} = 0, \end{cases} \tag{3.7}$$

or in vector notation using the definitions in Eqs. 3.1 and 3.2,

$$\mathbf{F}_{I/R,J} + \mathbf{F}_{T,J} + \mathbf{F}_{S,J} = 0. \tag{3.8}$$

Since $\mathbf{F}_{I/R,J}$ results from the superposition of incident and reflected waves, it can be split into indicent and reflected components, yielding

$$\mathbf{F}_{I,J} + \mathbf{F}_{R,J} + \mathbf{F}_{T,J} + \mathbf{F}_{S,J} = 0. \tag{3.9}$$

This force balance equation can be expressed in terms of the corresponding particle velocity components and generalized impedances. If $\mathbf{Z}_S$ is the generalized impedance representing the total response of waves traveling up and down the stiffener, and $\mathbf{Z}_{0,I}$, $\mathbf{Z}_{0,R}$, and $\mathbf{Z}_{0,T}$ are the characteristic generalized impedance of incident, reflected, and transmitted waves respectively, then by substitution into Eq. 3.9,

$$\mathbf{Z}_{0,I}\dot{\mathbf{u}}_{I,J} + \mathbf{Z}_{0,R}\dot{\mathbf{u}}_{R,J} + \mathbf{Z}_{0,T}\dot{\mathbf{u}}_{T,J} + \mathbf{Z}_S\dot{\mathbf{u}}_{S,J} = 0. \tag{3.10}$$

$\dot{\mathbf{u}}_{I/R,J}$ here has been split by superposition into it's right- and left-moving component,

$$\dot{\mathbf{u}}_{I/R,J} = \dot{\mathbf{u}}_{I,J} + \dot{\mathbf{u}}_{R,J}. \tag{3.11}$$

Displacements must also be continuous at the junction, so that

$$\dot{\mathbf{u}}_{T,J} = \dot{\mathbf{u}}_{S,J} = \dot{\mathbf{u}}_{I,J} + \dot{\mathbf{u}}_{R,J}. \tag{3.12}$$

Using this fact, substitution and rearrangement of Eq. 3.10, noting that $\mathbf{Z}_{0,I} = -\mathbf{Z}_{0,T}$ if the plates on the left and right are the same, yields

$$\dot{\mathbf{u}}_{R,J} = -\left(\mathbf{Z}_{0,R} + \mathbf{Z}_{0,T} + \mathbf{Z}_S\right)^{-1} \mathbf{Z}_S \dot{\mathbf{u}}_{I,J}. \tag{3.13}$$

Putting this equation in terms of incident and transmitted waves according to Eq. 3.11 yields

$$\dot{\mathbf{u}}_T = \left(\mathbf{I} - \left(\mathbf{Z}_{0,R} + \mathbf{Z}_{0,T} + \mathbf{Z}_S\right)^{-1} \mathbf{Z}_S\right) \dot{\mathbf{u}}_I, \tag{3.14}$$

which, after rearrangement, becomes

$$\dot{\mathbf{u}}_T = \left(\mathbf{Z}_{0,R} + \mathbf{Z}_{0,T} + \mathbf{Z}_S\right)^{-1} \left(\mathbf{Z}_{0,R} + \mathbf{Z}_{0,T}\right) \dot{\mathbf{u}}_I. \tag{3.15}$$

Equation 3.15 expresses transmitted particle velocities in terms of incident particle velocities and impedances. As is the case for most wave problems in bounded media though, guided plate waves occur in a discrete set of modes.

3.3.7 Plate waves

The theory of guided plate waves is well known and studied (15; 9). The exact theory due to Lamb describes dispersion of guided waves in a linear elastic isotropic plate. Figure 3.3 shows the dispersion curves of the first three guided Lamb modes for a 6061-T6 aluminum alloy plate with measured longitudinal wave speed $6242\,\mathrm{m/s}$, measured transverse wave speed $3144\,\mathrm{m/s}$, density $2700\,\mathrm{kg/m^3}$, and thickness $3.175\,\mathrm{mm}$. The real component of the complex wavenumber, corresponding to transmitted waves, is plotted in the right half-plane, and the imaginary component, corresponding to spatially decaying disturbances, is plotted in the left half-plane. This work makes use of the first two antisymmetric modes, A_0 and A_1, as well as
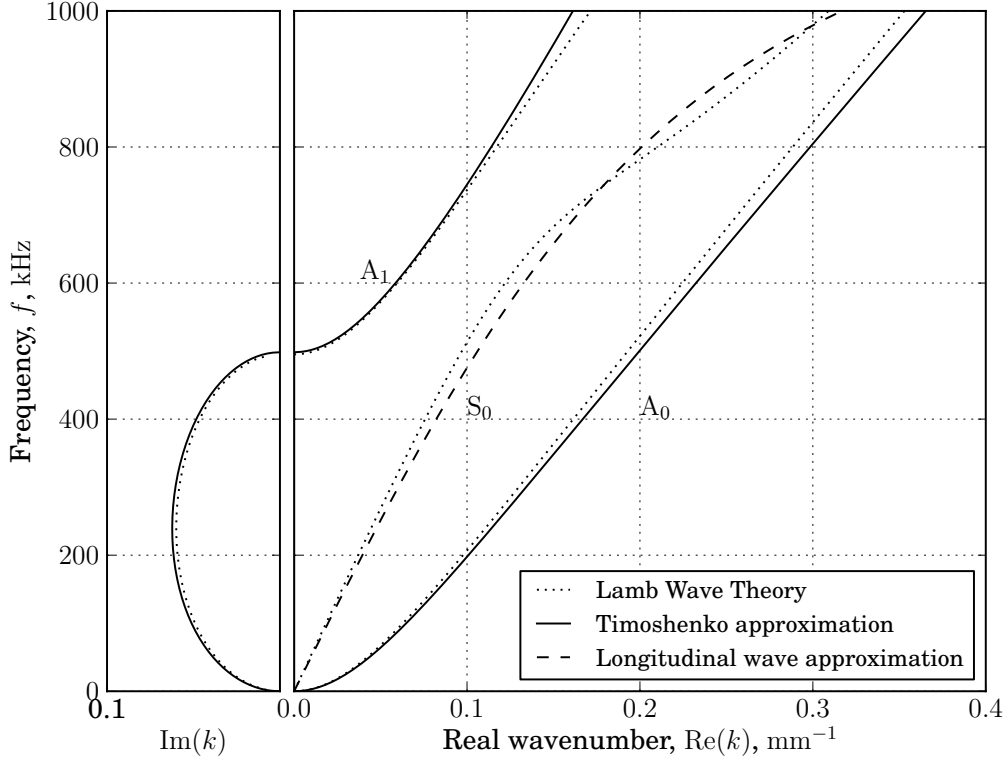
Figure 3.3   Dispersion curves for Lamb wave theory, along with Timoshenko and longitudinal wave approximations.

the first symmetric mode, S_0. At frequencies of interest in this work, the A_1 mode is a strictly evanescent (imaginary wavenumber) mode localized around a boundary.

The transmission formula in Eq. 3.15 is not dependent on which guided wave theory is used, except to the extent that a guided wave theory is needed to evaluate the impedance matrices. In the case of the approximate theories, these forces and moments take the form of a single expression corresponding to the traveling wave, as outlined in Appendix A. For the exact Lamb wave theory, integration across the cross section would be required to evaluate the total forces acting on the plate cross section from the Lamb wave modal amplitudes, giving

resultant normal force F, shear force V and moment M per depth

$$F = \int_{-d/2}^{d/2} \sigma_{xx}\, dy \tag{3.16}$$

$$V = \int_{-d/2}^{d/2} \sigma_{xy}\, dy \tag{3.17}$$

$$M = \int_{-d/2}^{d/2} \sigma_{xx} y\, dy, \tag{3.18}$$

where d is the thickness of the plate, x is the direction in the plane of the plate, and y is the lateral direction.

The work in this paper uses the approximate theory of Timoshenko for flexural waves and the approximate longitudinal wave solution. The longitudinal wave theory is modified to include the effect of lateral intertia due to the Poisson effect. Since the approximate theories in Fig. 3.3 overestimate the wavenumbers of all three modes in the 0-500 kHz range, a scalar correction factor of 0.965 is applied to all wavenumbers. The overestimate is due to the lack of rotational inertia, and the scalar correction makes it possible to produce very accurate wavespeed-sensitive results even while using the very simple approximate theories. A comparison of results obtained with the exact Lamb wave theory is presented in Appendix A.

Similarly, displacements and their time derivatives are evaluated from one of the guided wave theories. Timoshenko and the approximate longitudinal wave theory allow direct evaluation of rotation and displacement, while for exact Lamb wave theory, the rotation and horizontal and vertical displacements would be evaluated along the centerline of the plate.

By linearity, all of the guided wave theories give a simple proportionality between displacement and modal amplitude. In general, this may be written as

$$\dot{\mathbf{u}}_* = \mathbf{C}_* \boldsymbol{\xi}_* \tag{3.19}$$

where $*$ is one of I (incident), R (reflected), or T (transmitted), representing any one of the

traveling wave components in the problem. $\boldsymbol{\xi}$ here is a vector containing the amplitudes of the A_0, S_0, and A_1 modes, and $\mathbf{C}$ is a 3×3 matrix that follows from direct evaluation of displacement amplitudes given modal amplitudes. Assuming the left and right plates are the same, $\mathbf{C}_I = \mathbf{C}_T$ since the waves in each are both right-moving, so that Eqs. 3.13 and 3.15 become, through substitution of 3.19,

$$\boldsymbol{\xi}_T = \mathbf{C}_I^{-1} \left(\mathbf{Z}_{0,R} + \mathbf{Z}_{0,T} + \mathbf{Z}_S \right)^{-1} \left(\mathbf{Z}_{0,R} + \mathbf{Z}_{0,T} \right) \mathbf{C}_I \boldsymbol{\xi}_I \tag{3.20}$$

$$\boldsymbol{\xi}_R = \mathbf{C}_R^{-1} \left(\mathbf{Z}_{0,R} + \mathbf{Z}_{0,T} + \mathbf{Z}_S \right)^{-1} \mathbf{Z}_S \mathbf{C}_I \boldsymbol{\xi}_I. \tag{3.21}$$

Equation 3.3.7 determines the amplitudes of transmitted Lamb wave components from the incident amplitudes, while Eq. 3.21 determines the amplitude of reflected Lamb wave components. A number of conclusions follow from Eq. 3.3.7 even without direct evaluation of the impedances. As the stiffener becomes small or at resonence when $\mathbf{Z}_S$ vanishes, all terms on the righthand side of equation except for $\boldsymbol{\xi}_I$ cancel, making the transmitted amplitude equal to the incident amplitude, as would be expected if the stiffener were not there. When the stiffener impedance becomes large relative to the characteristic impedance of the plate (between resonances), the righthand side becomes zero and indicates pure reflection of energy from the stiffener.

It turns out that, accounting for the sign changes that occur when the mirror image of transmitted wave forces and displacements is compared to reflected forces and displacements, all of the off-diagonal elements of $\mathbf{Z}_{0,R} + \mathbf{Z}_{0,T}$ cancel, while the diagonal components are equal and add constructively. Thus only the diagonal elements of the generalized plate impedance, $H/\dot{u}$, $V/\dot{v}$, and $M/\dot{\theta}$, affect the transmission coefficient.

3.4   Calculation of Generalized Impedance

Within the bounds of the approximations, the modal transmission and reflection coefficients in Eqs. 3.3.7 and 3.21 present a very simple, concise solution to the complicated stiffener transmission problem. They provide the means to calculate transmitted and reflected amplitudes from just the characteristic impedance of the plate and the impedance of the stiffener. All complexity is contained within the impedances, which must now be calculated.

3.4.1   Characteristic Impedance of Plate Waves

Prescribing a set of particle velocities on a cut section of a plate uniquely determines the forces on the cross section by the traveling wave solutions. Thus prescribing a single horizontal particle velocity component $\dot{u}$ uniquely determines corresponding forces H, V, and M acting on the cross section. The most straightforward velocity is thus the unit vector $[\dot{u} = 1, \dot{v} = 0, \dot{\theta} = 0]^T$. The ratios between H, V, and M and particle velocity $\dot{u}$ respectively are the impedance matrix components z_{11}, z_{21}, and z_{31} as defined in Eq. 3.5. The second and third columns of the impedance matrix are determined by prescribing unit vectors in the $\dot{v}$ and $\dot{\theta}$ components respectively.

Figure 3.4 shows the nine elements of the characteristic generalized impedance matrix for right-moving waves, both incident ($\mathbf{Z}_{0,I}$) and transmitted ($\mathbf{Z}_{0,T}$). So that each of the nine elements are visible on the same vertical scale, each element is non-dimensionalized through *per-element* multiplication by

$$\frac{E}{\omega_0} \begin{bmatrix} 1 & 1 & d_p \\ 1 & 1 & d_p \\ d_p & d_p & d_p^2 \end{bmatrix} \tag{3.22}$$

where E is Young's modulus and ω_0 is a characteristic temporal frequency of the problem,
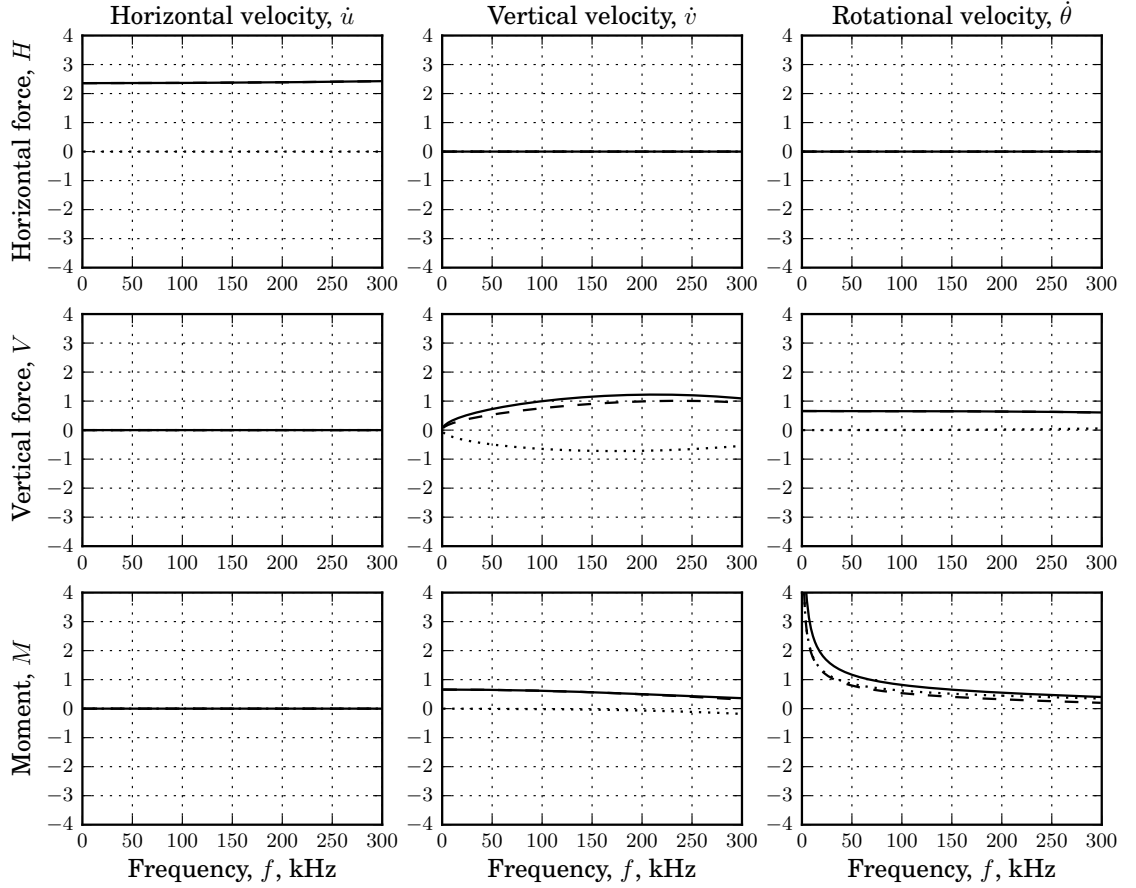
Figure 3.4   The nine non-dimensionalized elements of the characteristic generalized impedance
of incident waves, shown with real part (- -), imaginary part ($\cdots$), and modulus
(—).

chosen arbitrarily to be 100kHz for this geometry and material. Four of the elements in Fig. 3.4

are identically zero. They are identically zero because horizontal force and particle velocity

correspond to symmetric Lamb waves, whereas vertical/rotational forces/particle velocities

correspond to antisymmetric Lamb waves. Since symmetric and antisymmetric Lamb waves

are decoupled the impedance matrix must also be decoupled.

Characteristic impedance for reflected waves ($\mathbf{Z}_{0,R}$) are calculated by the same procedure.
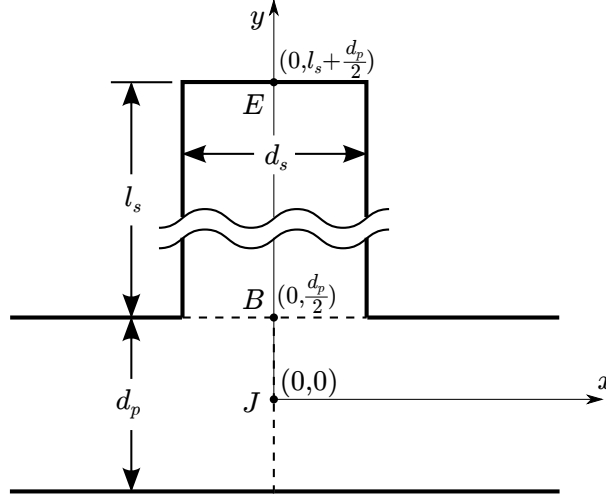
Figure 3.5   Coordinate system for the stiffener cross-section.

Results are the same as Fig. 3.4 except the $z_{2,3}$ and $z_{3,2}$ elements are negated because of the opposite propagation direction. For both right and left-moving waves, all of the impedance components are slowly varying as a function of frequency.

3.4.2   Stiffener Impedance

The impedance of the stiffener is calculated in a similar manner. The stiffener, however, has three extra constraints since there is no normal force, shear force, or moment acting on the free end of the stiffener. Figure 3.5 shows the coordinate system for the impedance calculation. The impedance if first calculated about the base of the stiffener, point B. To calculate the first column of the impedance matrix, a particle velocity vector in the $\dot{u}$ direction is prescribed at the base of the stiffener, the same as was done to calculate the characteristic impedance of the plate. Since there are wave components traveling up and down the plate however, there are six unknown wave amplitudes instead of the three wave amplitudes for waves travling a single direction in a plate. This means three extra equations are needed to solve for the forces at the base of the stiffener and calculate the impedance components. The three extra equations

come in the form of the stress-free condition at the free end of the stiffener. The equations $H_S(y) = 0$, $V_S(y) = 0$, and $M_S(y) = 0$ where $H_S(y)$, $V_S(y)$, and $M_S(y)$ are the traveling wave solutions for the horizontal force, vertical force, and moment in the stiffener, are evaluated at the free end of the stiffener. Together with the particle velocity equations at the base of the stiffener, these six equations are solved using computer algebra. This determines the three force components acting on the base of the stiffener, from which a single column of the impedance matrix is calculated. As for the plate, unit particle velocities in the $\dot{v}$ and $\dot{\theta}$ directions produce the other two columns.

In this manner, the impedance $\mathbf{Z}_{S,B}$ is first calculated about the base of the stiffener (point B). We treat the stiffener as only the material above the surface of underlying plate and will then extrapolate to determine an effective impedance at joint J, consistent with the forces at point J defined in Fig. 3.2. This perturbed impedance accounts for rotation of the base of the stiffener (point B) about the center of the junction (point J) due to the rotational component of the wave, and also accounts for shear and longitudinal strain in the stiffener.

Fig. 3.5 shows a cross section of the stiffener-plate combination. The plate has thickness d_p, and the stiffener has width d_s and height l_s. The dashed lines (- -) indicate the cuts that separate the domain into three regions: the incoming/reflected wave side to the left, the transmitted wave side to the right, and the stiffener.

The base of the stiffener applies a force to point B. To connect this to the impedance calculations of Eq. **??**, we need to replace it by an equivalent force applied to the center of the junction, point J. From the free body diagram, we consider the effect of force $\mathbf{F}_{S,B}$ at point J

by writing

$$\mathbf{F}_{S,J} = \begin{bmatrix} H_B \\ V_B \\ M_B - H_B\frac{d_p}{2} \end{bmatrix} = \underbrace{\begin{bmatrix} 1 & 0 & 0 \\ 0 & 1 & 0 \\ -\frac{d_p}{2} & 0 & 1 \end{bmatrix}}_{\mathbf{K}_1} \begin{bmatrix} H_B \\ V_B \\ M_B \end{bmatrix}, \tag{3.23}$$

where the moment is decreased by the shear force H_B times perpendicular distance $\frac{d_p}{2}$. The transformation can be represented as a matrix $\mathbf{K}_1$. In vector notation,

$$\mathbf{F}_{S,J} = \mathbf{K}_1\mathbf{F}_{S,B}. \tag{3.24}$$

For small plate thicknesses, $\mathbf{K}_1$ approaches the identity matrix.

We state particle velocity $\dot{\boldsymbol{u}}_{S,B}$ in terms of $\dot{\boldsymbol{u}}_{S,J}$ by first observering that vertical offset at the base of the stiffener leads to lateral motion when the plate rotates. In terms of displacements,

$$u_{S,B} = u_{S,J} - \frac{d_p}{2}\sin(\theta_{S,J}) \approx u_{S,J} - \frac{d_p}{2}\theta_{S,J}. \tag{3.25}$$

Longitudinal strain in the stiffener causes vertical displacement of the base of the stiffener,

$$v_{S,B} = v_{S,J} - \left.\frac{\partial v_S}{\partial y}\right|_B \cdot \frac{d_p}{2}, \tag{3.26}$$

and shear strain produces lateral displacement

$$u_{S,B} = u_{S,J} - \left.\frac{\partial u_S}{\partial y}\right|_B \cdot \frac{d_p}{2}. \tag{3.27}$$

Approximate continuity of rotation throughout the junction implies, simply,

$$\theta_{S,B} = \theta_{S,J}. \tag{3.28}$$

In matrix form, these modifications become

$$\begin{bmatrix} u_{S,B} \\ v_{S,B} \\ \theta_{S,B} \end{bmatrix} = \begin{bmatrix} u_{S,J} \\ v_{S,J} \\ \theta_{S,J} \end{bmatrix} + \begin{bmatrix} -\frac{d_p}{2}\theta_{S,J} \\ 0 \\ 0 \end{bmatrix} + \begin{bmatrix} -\left.\frac{\partial u_S}{\partial y}\right|_B \frac{d_p}{2} \\ 0 \\ -\left.\frac{\partial v_S}{\partial y}\right|_B \frac{d_p}{2} \\ 0 \end{bmatrix} \tag{3.29}$$

The first two vectors on the righthand side are easily combined by defining a perturbed identity matrix $\boldsymbol{K}_2$ to yield

$$
\begin{bmatrix} u_{S,B} \\ v_{S,B} \\ \theta_{S,B} \end{bmatrix} = \underbrace{\begin{bmatrix} 1 & 0 & -\frac{d_p}{2} \\ 0 & 1 & 0 \\ 0 & 0 & 1 \end{bmatrix}}_{\boldsymbol{K}_2} \begin{bmatrix} u_{S,J} \\ v_{S,J} \\ \theta_{S,J} \end{bmatrix} + \begin{bmatrix} -\frac{\partial u_S}{\partial y}\Big|_B \frac{d_p}{2} \\ -\frac{\partial v_S}{\partial y}\Big|_B \frac{d_p}{2} \\ 0 \end{bmatrix}.
\tag{3.30}
$$

Elimination of the last term follows from evaluation of the constituitive equation for normal force in the stiffener at point B. Starting with the constituitive equation,

$$
\sigma_{yy} = E\epsilon_{yy},
\tag{3.31}
$$

substitution of the parameters of this problem gives

$$
\frac{V_{S,B}}{d_s} = E \left.\frac{\partial v_S}{\partial y}\right|_B.
\tag{3.32}
$$

In a similar manner, the shear stress is put in terms of forces and displacements. The shear force is related to shear strain by

$$
\sigma_{xy} = 2G\epsilon_{xy}.
\tag{3.33}
$$

Similar substitution of forces and displacements gives

$$
\frac{H_{S,B}}{d_s} = 2G \left.\frac{\partial v_S}{\partial y}\right|_B.
\tag{3.34}
$$

Stated in terms of forces and differentiated in time, Eq. 3.30 becomes

$$
\dot{\boldsymbol{u}}_{S,B} = \boldsymbol{K}_2 \dot{\boldsymbol{u}}_{S,J} + \begin{bmatrix} -i\omega \frac{d_p}{d_s} \frac{H_{S,B}}{4G} \\ -i\omega \frac{d_p}{d_s} \frac{V_{S,B}}{2E} \\ 0 \end{bmatrix}.
\tag{3.35}
$$

Factorization again puts the equation in terms of known quantities, yielding

$$
\dot{\boldsymbol{u}}_{S,B} = \boldsymbol{K}_2 \dot{\boldsymbol{u}}_{S,J} + \underbrace{\begin{bmatrix} -i\omega \frac{d_p}{d_s} \frac{1}{4G} & 0 & 0 \\ 0 & -i\omega \frac{d_p}{d_s} \frac{1}{2E} & 0 \\ 0 & 0 & 0 \end{bmatrix}}_{\boldsymbol{K}_3} \boldsymbol{F}_{S,B}
\tag{3.36}
$$

Generalized stiffener impedance about point J is defined by

$$\boldsymbol{F}_{S,J} = \boldsymbol{Z}_{S,J}\dot{\boldsymbol{u}}_{S,J}. \tag{3.37}$$

Substituting Eq. 3.36 into Eq. 3.37,

$$\boldsymbol{K}_1^{-1}\boldsymbol{F}_{S,J} = \boldsymbol{Z}_{S,B}\left(\boldsymbol{K}_2\dot{\boldsymbol{u}}_{S,J} + \boldsymbol{K}_3\boldsymbol{F}_{S,B}\right), \tag{3.38}$$

and rearranging yields the desired relation between $\boldsymbol{F}_{S,J}$ and $\dot{\boldsymbol{u}}_{S,J}$,

$$\boldsymbol{F}_{S,J} = \underbrace{\left(\boldsymbol{I} - \boldsymbol{K}_1\boldsymbol{Z}_{S,B}\boldsymbol{K}_3\boldsymbol{K}_1^{-1}\right)^{-1}\boldsymbol{K}_1\boldsymbol{Z}_{S,B}\boldsymbol{K}_2}_{\boldsymbol{Z}_{S,J}}\,\dot{\boldsymbol{u}}_{S,J}, \tag{3.39}$$

$$\boldsymbol{F}_{S,J} = \boldsymbol{Z}_{S,J}\dot{\boldsymbol{u}}_{S,J}, \tag{3.40}$$

where $\boldsymbol{I}$ is the identity matrix and $\boldsymbol{Z}_{S,J}$ is the resulting perturbed stiffener impedance matrix. Note that as d_p in K_2 and K_3 approaches zero, $\boldsymbol{Z}_{S,J}$ approaches the unperturbed $\boldsymbol{Z}_{S,B}$.

Fig. 3.6 shows all nine elements of the stiffener impedance $\boldsymbol{Z}_{S,J}$, plotted as a function of frequency and with the same normalization as for Fig. 3.4. The strictly imaginary impedances indicate a purely reactive stiffener that transmits no net power into or out of the stiffener. The most obvious difference compared to the characteristic impedance of the plate is the presence of sharp peaks in all nonzero elements. These points of large impedance correspond to resonances of the A_0 or S_0 modes traveling up and down in the stiffener. The '$\times$' shape of nonzero elements in $\boldsymbol{Z}_{S,J}$ reflects decoupling of vertical force/particle velocity from horizontal/rotational forces/particle velocities. The interchange between horizontal and vertical between the plate and stiffener switches which component is decoupled. It is this difference that drives the mode conversion at low frequencies.
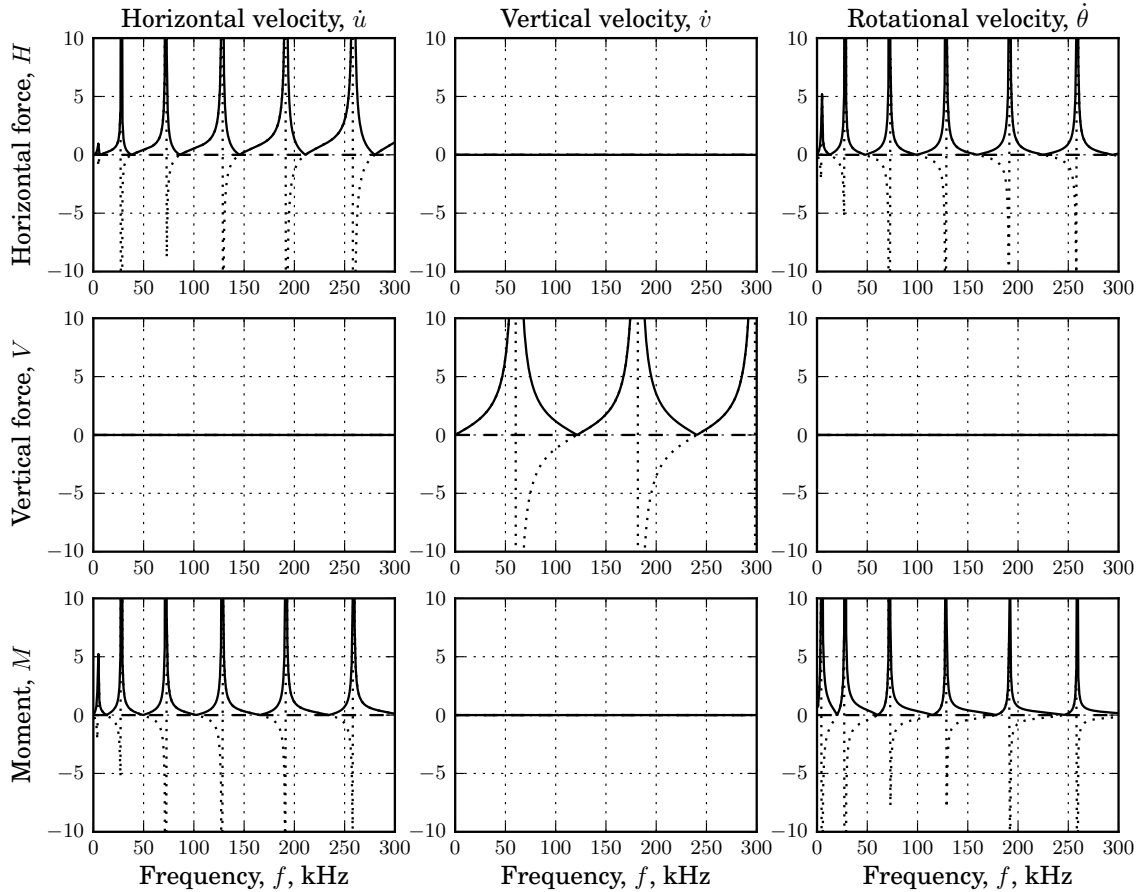
Figure 3.6 The nine non-dimensionalized elements of the stiffener impedance, $\mathbf{Z}_S$, shown with real part (- -), imaginary part ($\cdots$), and modulus (—).

3.5   Results

Impedances are calculated using the approximate Timoshenko flexural and longitudinal wave theories, and computations are performed for a plate with thickness 3.175 mm and a stiffener with height 21.97 mm and width 2.54 mm. Material properties correspond to a specimen of 6061-T6 aluminum alloy with measured longitudinal wave speed $6242\,\mathrm{m/s}$, transverse wave speed $3144\,\mathrm{m/s}$, and density $2700\,\mathrm{kg/m^3}$.

Figure 3.7 S_0 energy reflection and transmission coefficients for incident S_0 Lamb waves. Deformed shapes for lettered points plotted in Fig. 3.8.

3.5.1 S_0 Transmission

Figure 3.7 shows the magnitude of the S_0 energy transmission coefficient $T_{S_0}(\omega)$, defined as

$$T_{S_0}(\omega) = \left| \frac{\xi_{T,S_0}(\omega)}{\xi_{I,S_0}(\omega)} \right|^2 , \tag{3.41}$$

where $\xi_{T,S_0}(\omega)$ represents the frequency-dependent modal amplitude of the transmitted S_0 waves and $\xi_{I,S_0}(\omega)$ represents the modal amplitude of incident S_0 waves. The transmission shows a periodicity of roughly 55 kHz, corresponding to the spacing between resonant frequencies of flexural motion in the stiffener. Maximum transmission peaks at resonances with a transmission coefficient near 1.0, and the stiffener blocks as much as 70% of the incident energy in the S_0 mode between resonances. The energy that is not transmitted as S_0 is split between reflected S_0 and mode-converted reflected and transmitted A_0.

Figure 3.8 (a)-(e) shows instantaneous deformed shapes calculated from evaluation of the traveling wave solutions at several frequencies for incident S_0 waves. The corresponding frequencies are labeled by letter in Fig. 3.7. The incident S_0 mode is dominated by lateral motion

Figure 3.8   Instantaneous deformed shapes for S_0 Lamb waves incident from the left at frequencies 50 kHz (a), 70 kHz (b), 95 kHz (c), 120 kHz (d), and 150 kHz (e).
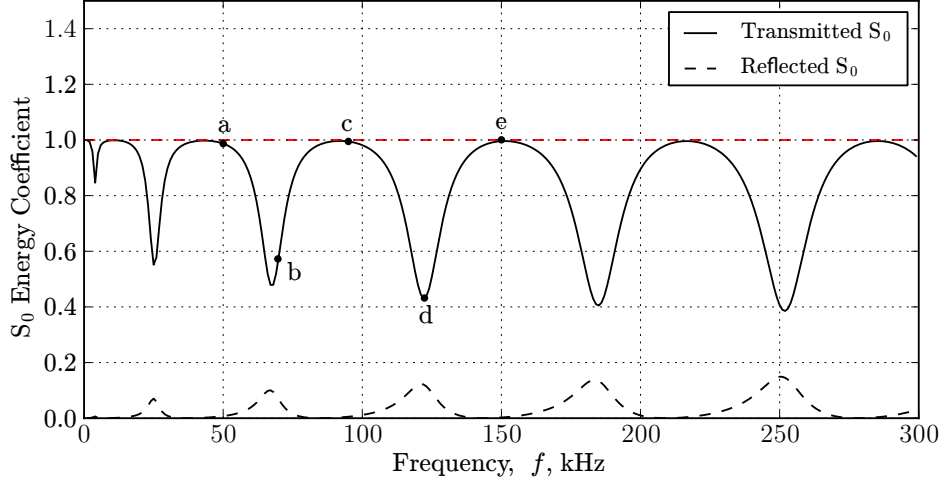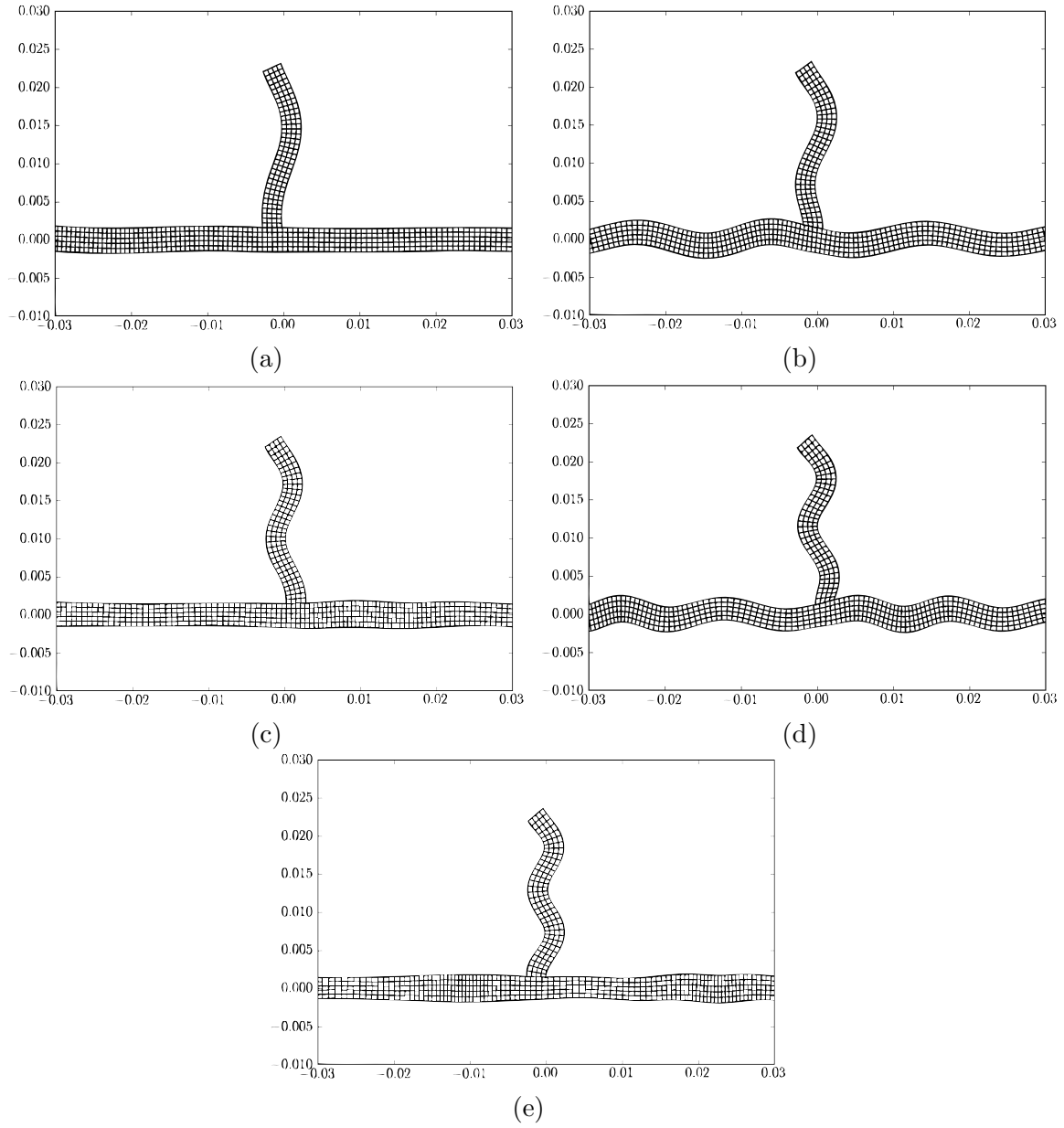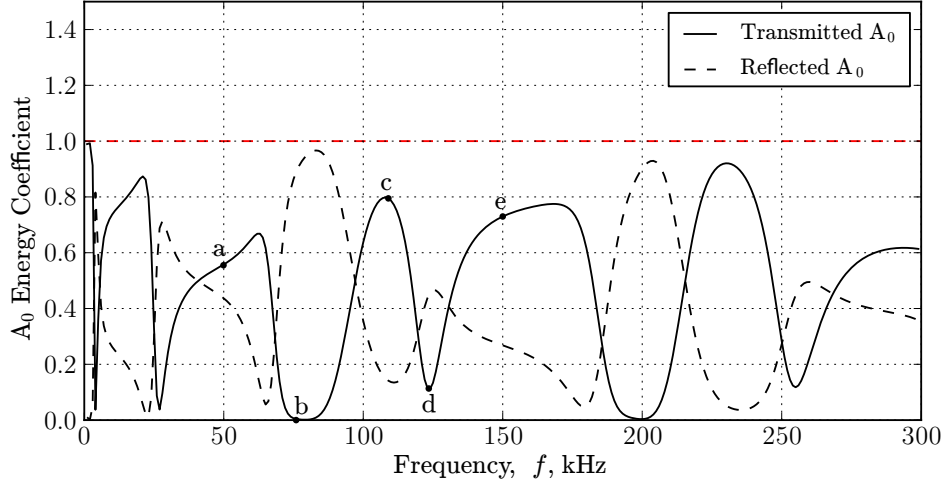
Figure 3.9 A_0 energy reflection and transmission coefficients for incident A_0 Lamb waves. Deformed shapes for lettered points plotted in Fig. 3.11.

which excites flexural waves in the stiffener. The S_0 incident and transmitted waves are virtually invisible in Fig. 3.8 because their displacements are so much less than for the A_0 waves. The waves visible in Fig. 3.8 are the reflected mode-converted A_0 on the left, the transmitted mode-converted A_0 on the right, and A_0 coupled into the stiffener. Transmission is determined by stiffener resonance. The number of flexural wavelengths that fit in the stiffener increases with frequency. In Figs. 3.8 (a), (c), and (e), the stiffener exhibits an approximately pure flexural resonant mode of 2nd, 3rd, and 4th order, respectively. This occurs at frequencies for which the impedance of the A_0 mode in the stiffener is small. These frequencies can be identified in Fig. 3.6 where the inpedances in the four corner elements of the impedance matrix approach are small. These frequency bands correspond to high S_0 transmission. At the alternate frequencies plotted in Figs. 3.8 (b) and (d), the stiffener exhibits high impedance and blocks transmission of the S_0 mode.

3.5.2 A_0 Transmission

Figure 3.9 shows the magnitude of the A_0 energy transmission coefficient $T_{A_0}(\omega)$, defined as

$$T_{S_0}(\omega) = \left| \frac{\xi_{T,S_0}(\omega)}{\xi_{I,S_0}(\omega)} \right|^2, \tag{3.42}$$

where $\xi_{T,A_0}(\omega)$ represents the frequency-dependent modal amplitude of the transmitted A_0 waves and $\xi_{I,A_0}(\omega)$ represents the modal amplitude of incident A_0 waves. Similar to the case of incident S_0, the transmission shows a periodicity of roughly 55 kHz, but the pattern of A_0 transmission is significantly more complex due to the coupling between lateral and rotation motion in the A_0 mode. The reflection and transmission coefficients plotted in Fig. 3.9 show alternating bands of high and low transmission, but unlike the S_0 transmission coefficients of Fig. 3.7, the regularity is not immediately apparent. In the case of incident A_0 waves, vertical motion in the A_0 mode couples into longitudinal waves in the stiffener, and rotational motion in the A_0 mode couples into flexural waves in the stiffener, thus both the longitudinal and flexural stiffener resonances may impede energy transmission. This is seen in Fig. 3.9 as *alternating* bands of low and very low transmission. The very low transmission bands centered around 75 and 195 kHz correspond to flexural and longitudinal impedance peaks, while the moderately low transmission bands around 120 and 250 kHz correspond to only longitudinal stiffener impedance peaks. The approximate overlap of A_0 and S_0 resonances is a result of the approximate 2:1 ratio in wavespeeds (phase velocities) between the A_0 and S_0 modes. In isotropic materials with a Poisson's ratio near 0.3, the 2:1 ratio holds below the cutoff frequency of the A_1 mode (approximately 500 kHz for this geometry and material).

Figure 3.10 shows a comparison of the model calculations for the transmission coefficient of

incident A_0 waves with a numerical boundary element code (5). The dotted line additionally shows experimental measurements performed on a plate with the same geometric and material properties (16). The model and numerical solutions show almost perfect agreement from 50-100 kHz, and agreement is very good up to roughly 200 kHz. Beyond 200 kHz, the solutions begin to diverge since the impedance model does not accurately model deformation of the junction. Both computations match the experimental data reasonably well, demonstrating very similar stopbands and passbands over the full frequency range. The deviation in precise shape can be attributed to limitations in the experimental measurements due to mode conversion and the finite extent of the plate (16). Despite the limitations of the approximation, it still provides a straightforward and accurate explanation of the physical mechanism behind the scattering problem.

For both incident A_0 and incident S_0, roughly $\frac{n}{2} + \frac{1}{4}$ wavelengths fit in the stiffener at resonance. These resonances result in the regions of high transmission. Conversely, a peak in the impedance of the flexural mode of the stiffener results in moderately low transmission (e.g. 25 kHz, 125 kHz, and 255 kHz in Fig. 3.9), and a peak in the impedance both the flexural and longitudinal modes of the stiffener results in a band of very low transmission (e.g. 75 kHz and 200 kHz in Fig. 3.9).

3.5.3 Conclusion

A model is developed for transmission and reflection of guided plate waves incident upon an integral stiffener. Using the impedance method with approximate guided wave theories, good agreement is demonstrated with numerical calculations and experimental data over a range of frequencies. Despite the simplicity of the model, it accurately reprouces the complex pass-
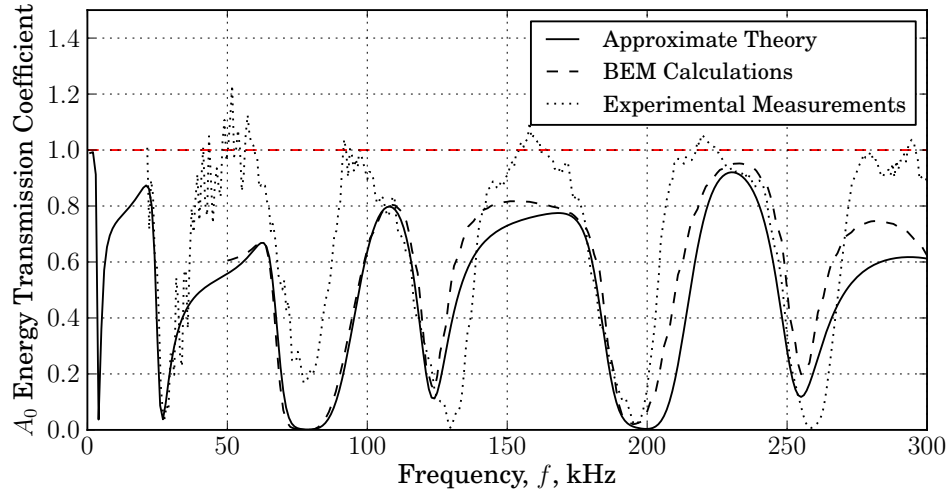
Figure 3.10   Comparison of A_0 energy transmission coefficient with numerical solution and experimental data for incident A_0 Lamb waves.

bands and stop-bands resulting from $\frac{n}{2} + \frac{1}{4}$ - wavelength flexural and longitudinal resonances in the stiffener. This explanation guides the designer in quickly determining frequencies where an integral stiffener is expected to either transmit or scatter guided waves incident at a normal angle.

Figure 3.11   Instantaneous deformed shapes for A_0 Lamb waves incident from the left at frequencies 50 kHz (a), 75 kHz (b), 110 kHz (c), 125 kHz (d), and 160 kHz (e).

Bibliography

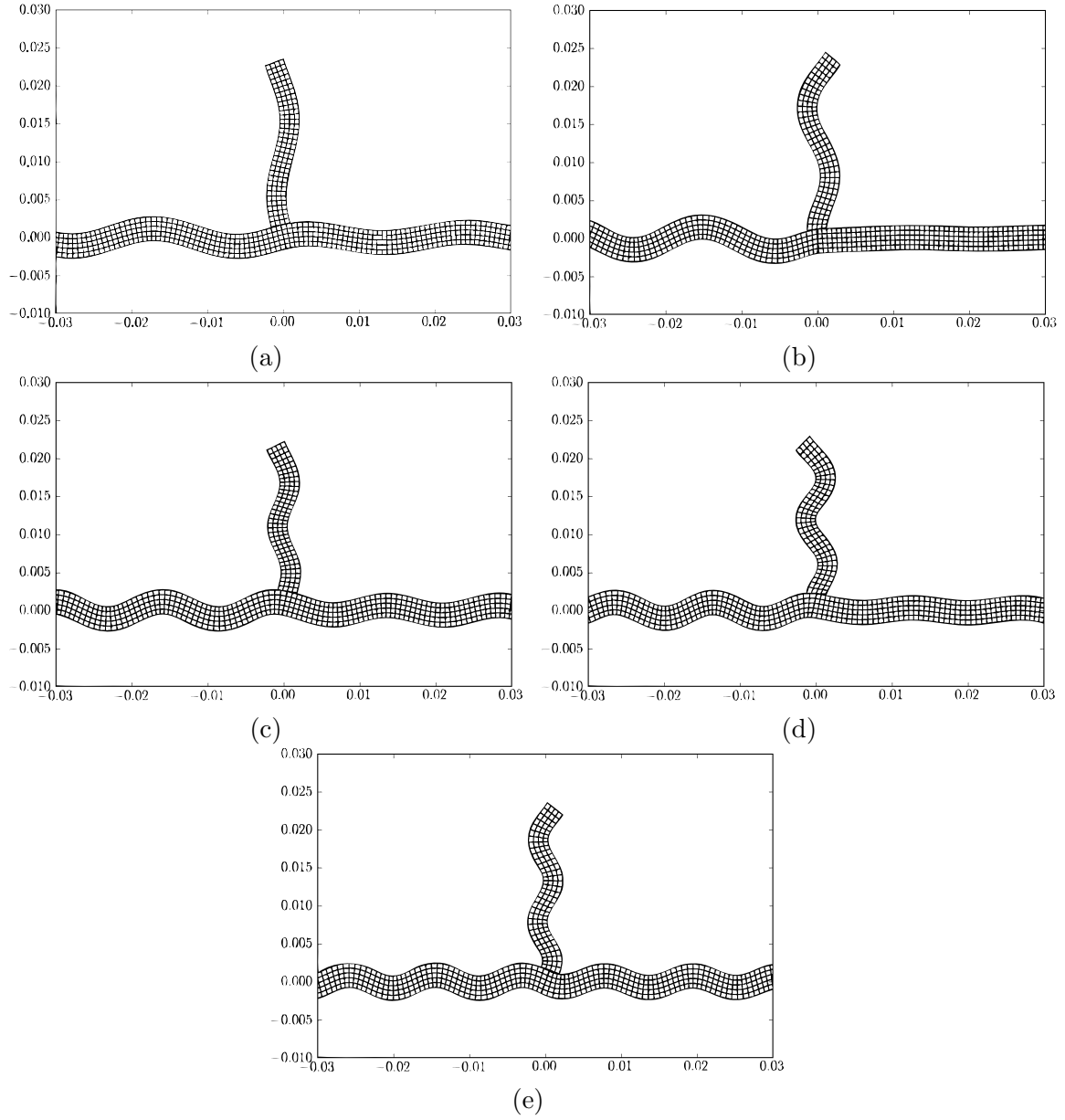[1] A. Raghavan, C. E. S. Cesnik, "Review of Guided-wave Structural Health Monitoring," *The Shock and Vibration Digest* **39**(2), pp. 91-114, (2007).

[2] A. Cheng, D. Cheng, "Heritage and early history of the boundary element method," *Engineering Analysis with Boundary Elements* **29**, pp. 268-302, (2005).

[3] J. D. Achenbach, *Reciprocity in Elastodynamics*, (Cambridge Univ Press, London, 2003).

[4] R. A. Roberts, "Guided wave propagation in integrally stiffened plates," in *Review of Progress in Quantitative Nondestructive Evaluation*, vol. 27, D. O. Thompson, D. E. Chimenti, Eds. (AIP Press, New York, 2008), pp. 170–177.

[5] R. A. Roberts, "Plate wave transmission/reflection at geometric obstructions: model study," *Review of Progress in Quantitative Nondestructive Evaluation*, vol. 29, D. O. Thompson, D. E. Chimenti, Eds. (AIP Press, New York, 2010), pp. 192–199.

[6] P. Wilcox, A. Velichko, B. Drinkwater, A. Croxford, "Scattering of plane guided waves obliquely incident on a straight feature with uniform cross-section," *J. Acoust. Soc. Am.* **128**(5), pp. 2715-2725, (2010).

[7] J. P. Lee, H. Kolsky, "The Generation of Stress Pulses at the Junction of Two Noncollinear Rods," *Journal of Applied Mechanics* **39**(3), pp. 809-814, (1972).

[8] K. J. Yong, K. J. Atkins, "Generation of elastic stress waves at a T-junction of square rods," *Journal of Sound and Vibration* **88**(4), pp. 431-436, (1983).

[9] J. D. Achenbach, *Wave propagation in elastic solids*, American Elselvier, (1973).

[10] Y. Cho, J. Rose, "A boundary element solution for a mode conversion study on the edge reflection of Lamb waves," *Journal of the Acoustical Society of America*, **99**(4), pp. 2097-2109, (1996).

[11] B. Morvan, N. Wilie-Chancellier, H. Duflo, A. Tinel, J. Duclos, "Lamb wave reflection at the free edge of a plate" in J. Acoust. Soc. Am. **113**(3), pp. 1417-1425, (2003).

[12] S. A. Martin, K. V. Jata, "FEM modeling of guided wave behavior in integrally stiffened plate structures," SPIE Proceedings, Vol. 6529, (2007).

[13] D. W. Greve, N. Tyson, I. J. Oppenheim, "Interaction of defects with Lamb waves in complex geometries," *IEEE Ultrasonics Conference Proceedings*, 297-300, (2005).

[14] W. C. Elmore, M. A. Heald, *Physics of Waves*, Dover Publications, (1985).

[15] K. Graff, *Wave Motion in Elastic Solids*, Dover Publications, (1991).

[16] R.S. Reusser, D.E. Chimenti, R.A. Roberts, S.D. Holland, "Guided plate wave scattering at vertical stiffeners and its effect on source location," ULTRASONICS, In Press, Accepted for Publication 26 October 2011.

CHAPTER 4.   Conclusions

4.1   Summary

The case of waves normally incident upon an integral stiffener has been studied in detail and the results have been applied to the problem of spacecraft leak location.

In the first part of this work, transmission of the A_0 guided wave mode normally incident upon a low and high aspect ratio stiffener is measured and related to performance of a leak location system for manned spacecraft. A pattern of high and low transmission frequency bands is observed. It is demonstrated that integral stiffeners acting as frequency-dependent filters limit the range of the leak location system. Although normal incidence upon a stiffener does not adequately describe guided wave interaction with the complex pattern of stiffeners, very good correlation is observed between normal transmission and the ability of a virtual detector to locate a synthetic leak source. Based on these observations, two algorithms are proposed for determing the best frequency band for detecting leak-generated noise. The first, termed *in-situ* calibration relies on virtual leak sources to determine *a posteriori* which narrow frequency bands produce acceptable results. The second, termed *wide bandwidth* calibration, simply uses all available frequencies. Wide bandwidth is determined to be the most robust option since most stiffeners have rapidly varying transmission peaks and valleys and so will not have a narrow frequency band that produces consistently acceptable results.

In the second part of this work, the mechanics of transmission past an integral stiffener at

normal incidence are examined in greater depth. Using approximate longitudinal and flexural wave theories, a model is developed that accurately predicts low-frequency transmission and reflection. For incident S_0 waves, it is found that high transmission corresponds to low stiffener mechanical impedance of flexural waves in the stiffener. Transmission of incident A_0 waves is found to depend on both the flexural and longitudinal resonances in the stiffener.

4.2   Recommendations for future research

Waves incident on a stiffener at an oblique angle have not been considered in this work. The relatively simple mechanics governing the problem of normal incidence suggest that a straightforward extrapolation is possible for angles of incidence close to normal. Wilcox (6) takes a detailed look at computational methods and physical mechanisms for waves obliquely incident on an adhesively bonded hollow square stiffener. The complexity of that problem means it requires numerical solution, but it should be possible to gain a deeper understanding of the somewhat simpler problem of waves obliquely incident on the integral stiffener considered in this work. This would be invaluable information for the designer who desires approximate guidelines rather than tabulated solutions for each possible case.

APPENDIX A.   APPROXIMATE GUIDED WAVE THEORY

Timoshenko flexural wave approximation

The Timoshenko beam theory approximation (15) applied to flexural waves in a plate captures the two lowest order flexural Lamb modes, the A_0 and A_1 modes. By accounting for the rotation of the cross-section, Timoshenko derives a theory that, while still quasi one-dimensional, closely approximates the exact Lamb wave solution.

A single traveling wave represents the solution, but the theory considers translation and rotation separately. Transverse displacement v is represented by

$$v = B_1 e^{i(kx - \omega t)}, \tag{A.1}$$

where $e^{i(kx - \omega t)}$ represents the traveling wave with wavenumber k and angular temporal frequency ω, and B_1 is an arbitrary coefficient defining the amplitude and phase of the wave. The key feature of Timoshenko flexural wave theory is that a second traveling wave defines the rotation ψ of the cross section plane, as opposed to the slope of the surface of the beam, $\frac{\partial v}{\partial x}$. ψ is defined as

$$\psi = B_2 e^{i(kx - \omega t)}, \tag{A.2}$$

and it is related to the traveling wave solution for v by the relation

$$\frac{B_2}{B_1} = i \frac{(G\kappa k^2 - \rho\omega^2)}{G\kappa k}. \tag{A.3}$$

Here, κ is the so-called shear coefficient, given as 0.833 for rectangular cross-sections. ρ is the density of the material, and G is the shear modulus. Note that as $\omega \to 0$, $\frac{B_2}{B_1} \to ik$, or a simple derivative. Correspondingly, Timoshenko defines the moment and shear forces per depth acting on a cross section of the plate as

$$M = -EI\frac{\partial \psi}{\partial x} \tag{A.4}$$

and

$$V = \frac{\partial M}{\partial x} + \rho I \frac{\partial^2 \psi}{\partial t^2}. \tag{A.5}$$

From page 184 of Graff (15), the dispersion relation for these waves is

$$\frac{EI}{\rho A}k^4 - \frac{I}{A}\left(1 + \frac{E}{G\kappa}\right)k^2\omega^2 - \omega^2 + \frac{\rho I}{GA\kappa}\omega^4 = 0, \tag{A.6}$$

where κ is the so-called shear coefficient, with a value of 0.833 given for rectangular beam cross-sections, and A is the area of the cross-section. This theory applies to plates as well as beams since a plate is equivalent to a beam where everything has been scaled to unit depth.

Fig. 3.3 shows the result of Timoshenko's approximation. Since Eq. A.6 is a fourth-order polynomial in k, there are four corresponding roots. Two pairs differing only in sign correspond to solutions oriented in opposite directions. For each pair, one root corresponds to the the lowest order antisymmetric Lamb mode, A_0, while the other corresponds to the second lowest order antisymmetric Lamb mode, A_1. At low frequencies, the branch corresponding to the A_1 mode is purely complex, indicating a non-propagating mode. Fig. 3.3 shows one pair of roots with purely real wavenumbers in the right half-plane and purely imaginary wavenumbers in the left half-plane.

Approximate longitudinal Wave Theory

Graff (15) uses a variational approach to account for the effect of lateral inertia on longitudinal waves traveling in a bar. Unlike the flexural waves for which a rectangular bar was equivalent to a plate, Graff's derivation for longitudinal waves must be ammended to account for lateral inertia in only one direction rather than two. These straightforward modifications produce a modified partial differential equation for longitudinal waves in a plate,

$$\frac{\partial^2 u}{\partial x^2} + \left(\frac{\nu}{1-\nu}\right)^2 \frac{h^2}{12c_0^2}\frac{\partial^4 u}{\partial x^2 \partial t^2} = \frac{1}{c_0^2}\frac{\partial^2 u}{\partial t^2}. \tag{A.7}$$

Substitution of a traveling wave produces the corresponding dispersion relation,

$$\frac{h^2 k^2 \nu \omega^2}{12\left(\nu-1\right)} + c_0^2 k^2 = \omega^2. \tag{A.8}$$

Since this dispersion relation is only a second order polynomial, there are just two branches, corresponding to S_0 symmetric Lamb modes traveling in opposite directions.

Fig. 3.3 shows the approximate Timoshenko and longitudinal wave theories, along with the exact Lamb wave solution. Despite the approximations, all modes are approximated to within a wavenumber of about three percent all frequencies.

Traveling wave solutions

The approximate wave theories are expressed as traveling waves. Displacements are defined for each of the wave components (incident, reflected, transmitted, up the stiffener, and down the stiffener). For waves incident on the stiffener, the horizontal displacement u_I and vertical displacement v_I are

$$u_I = S_{0,I}e^{i(k_{S_0,P}x - \omega t)} \tag{A.9}$$

$$v_I = A_{0,I}e^{i(k_{A_0,P}x - \omega t)} + A_{1,I}e^{i(k_{A_1,P}x - \omega t)}, \tag{A.10}$$

where $A_{0,I}$, $S_{0,I}$, and $A_{1,I}$ represent the complex amplitudes of the incoming wave modes. Correspondingly, $k_{A_{0,P}}$, $k_{S_{0,P}}$, and $k_{A_{1,P}}$ represent the wavenumbers of each of the three modes in the plate. The reflected wave displacements are

$$u_R = S_{0,R}e^{i(-k_{S_{0,P}}x-\omega t)} \tag{A.11}$$

$$v_R = A_{0,R}e^{i(-k_{A_{0,P}}x-\omega t)} + A_{1,R}e^{i(-k_{A_{1,P}}x-\omega t)}, \tag{A.12}$$

so that the total displacement of the left half-plate is, by superposition,

$$u_{I/R} = u_I + u_R \tag{A.13}$$

$$v_{I/R} = v_I + v_R \tag{A.14}$$

Multiplying each term of the vertical displacement summation by its corresponding B_2/B_1 from Eq. A.3 determines the quantity $\psi_{I/R}$. Note that since B_2/B_1 is a function of k, the appropriate wavenumber of each term must be substituted into the expression for B_2/B_1.

The transmitted waves displacements u_T and v_T are similarly represented as

$$u_T = S_{0,T}e^{i(k_{S_{0,P}}x-\omega t)} \tag{A.15}$$

$$v_T = A_{0,T}e^{i(k_{A_{0,P}}x-\omega t)} + A_{1,T}e^{i(k_{A_{1,P}}x-\omega t)}, \tag{A.16}$$

and analogous term-by-term multiplication by B_2/B_1 yields an expression for ψ_T. Finally, the stiffener displacements u_S and v_S are

$$u_S = A_{0,U}e^{i(k_{A_{0,S}}x-\omega t)} + A_{0,D}e^{i(-k_{A_{0,S}}x-\omega t)} \tag{A.17}$$

$$+A_{1,U}e^{i(k_{A_{1,S}}x-\omega t)} + A_{1,D}e^{i(-k_{A_{1,S}}x-\omega t)}$$

$$v_S = S_{0,U}e^{i(k_{S_{0,S}}x-\omega t)} + S_{0,D}e^{i(-k_{S_{0,S}}x-\omega t)}, \tag{A.18}$$

where the U and D subscripts represent waves traveling up and down the stiffener, respectively, and the S subscript on the wavenumbers indicate wavenumbers of the three modes in a stiffener

with width d_s. Note that u_S and v_S are still represent horizontal and vertical displacements, respectively, so where flexural modes show up in the vertical displacement of the plate, they now show up in horizontal displacement of the stiffener.

The slope of the plate in Timoshenko's flexural wave theory, defined here as α, are for each of the sections,

$$\alpha_{I/R} = \frac{\partial v_{I/R}}{\partial x} \tag{A.19}$$

$$\alpha_T = \frac{\partial v_T}{\partial x} \tag{A.20}$$

$$\alpha_S = -\frac{\partial u_S}{\partial y}. \tag{A.21}$$

Sign conventions have been selected so that positive α corresponds to a counterclockwise rotation for each of the three plate sections. Since α represents the slope of the plate and ψ represents the rotation of the cross-section plane, they are averaged to get the rotation of a differential element of the material. Defining this rotation as θ,

$$\theta_{I/R} = \frac{1}{2}\left(\psi_{I/R} + \alpha_{I/R}\right) \tag{A.22}$$

$$\theta_T = \frac{1}{2}\left(\psi_T + \alpha_T\right) \tag{A.23}$$

$$\theta_S = \frac{1}{2}\left(-\psi_S + \alpha_S\right). \tag{A.24}$$

Fig. 3.2 illustrates the forces and moments acting on each of the cut sections. The normal stresses acting on the span of a cut section are

$$\sigma_{I/R} = E\frac{\partial u_{I/R}}{\partial x} \tag{A.25}$$

$$\sigma_T = E\frac{\partial u_T}{\partial x} \tag{A.26}$$

$$\sigma_S = E\frac{\partial v_S}{\partial y}, \tag{A.27}$$

so that the forces per unit depth are

$$F_{I/R} = \frac{\partial u_{I/R}}{\partial x} d_p \tag{A.28}$$

$$F_T = \frac{\partial u_T}{\partial x} d_p \tag{A.29}$$

$$F_S = \frac{\partial v_S}{\partial y} d_s. \tag{A.30}$$

The moments acting on the span of a cut section are, according to Eq. A.4,

$$M_{I/R} = \frac{1}{12} \frac{\partial \psi_{I/R}}{\partial x} E d_p^3 \tag{A.31}$$

$$M_T = \frac{1}{12} \frac{\partial \psi_T}{\partial x} E d_p^3 \tag{A.32}$$

$$M_S = \frac{1}{12} \frac{\partial \psi_S}{\partial y} E d_s^3 \tag{A.33}$$

Finally the shear forces acting on the span of a cut section are, according to Eq. A.5 and

Eqs. A.31–A.33,

$$V_{I/R} = \frac{\partial M_{I/R}}{\partial x} + \frac{1}{12} \frac{\partial \psi_{I/R}}{\partial t^2} \rho d_p^3 \tag{A.34}$$

$$V_T = \frac{\partial M_T}{\partial x} + \frac{1}{12} \frac{\partial \psi_T}{\partial t^2} \rho d_p^3 \tag{A.35}$$

$$V_S = -\frac{\partial M_S}{\partial y} + \frac{1}{12} \frac{\partial \psi_S}{\partial t^2} \rho d_s^3 \tag{A.36}$$

The preceeding equations have been reproduced in their entirety if only to emphasize exactly

where the unexpected sign differences occur. The negative signs arise naturally from the fact

that, while preserving horizontal and vertical displacements make vector addition simple, it

forces the stiffener into a left-handed coordinate system while the plate instead has a right-

handed coordinate system.

Comparison to approximate model with Lamb wave theory

To verify that the improved agreement is meaningful, the calculations discussed above are replicated with the Lamb wave model in place of approximate theories. Particle velocities are evaluated at the centerline of the plate, and the rotation is calculated directly from the field solution evaluated at the centerline,

$$\theta = \frac{1}{2} \left(\nabla \times \mathbf{u} \right). \tag{A.37}$$

The forces are evaluated by direct evaluation of stresses and integration across the span of the plate, giving forces and moments per unit depth in the plate of

$$F = \int_{-\frac{d_p}{2}}^{\frac{d_p}{2}} \sigma_{xx} \, dy \tag{A.38}$$

$$V = \int_{-\frac{d_p}{2}}^{\frac{d_p}{2}} \sigma_{xy} \, dy \tag{A.39}$$

$$M = \int_{-\frac{d_p}{2}}^{\frac{d_p}{2}} y \sigma_{xx} \, dy \tag{A.40}$$

The rest of the calculation proceeds as above and produces the transmission coefficients in Fig. A.1.

Fig. A.1 shows the energy transmission coefficient, defined as the squared magnitude of the transmitted A_0 mode amplitude given a pure unit-amplitude A_0 incident wave. The approximate model is plotted together with the results of the Boundary Element Method (BEM) simulation. Scaling the wavenumber by 0.965 as described above clearly improves agreement with the numerical simulation.
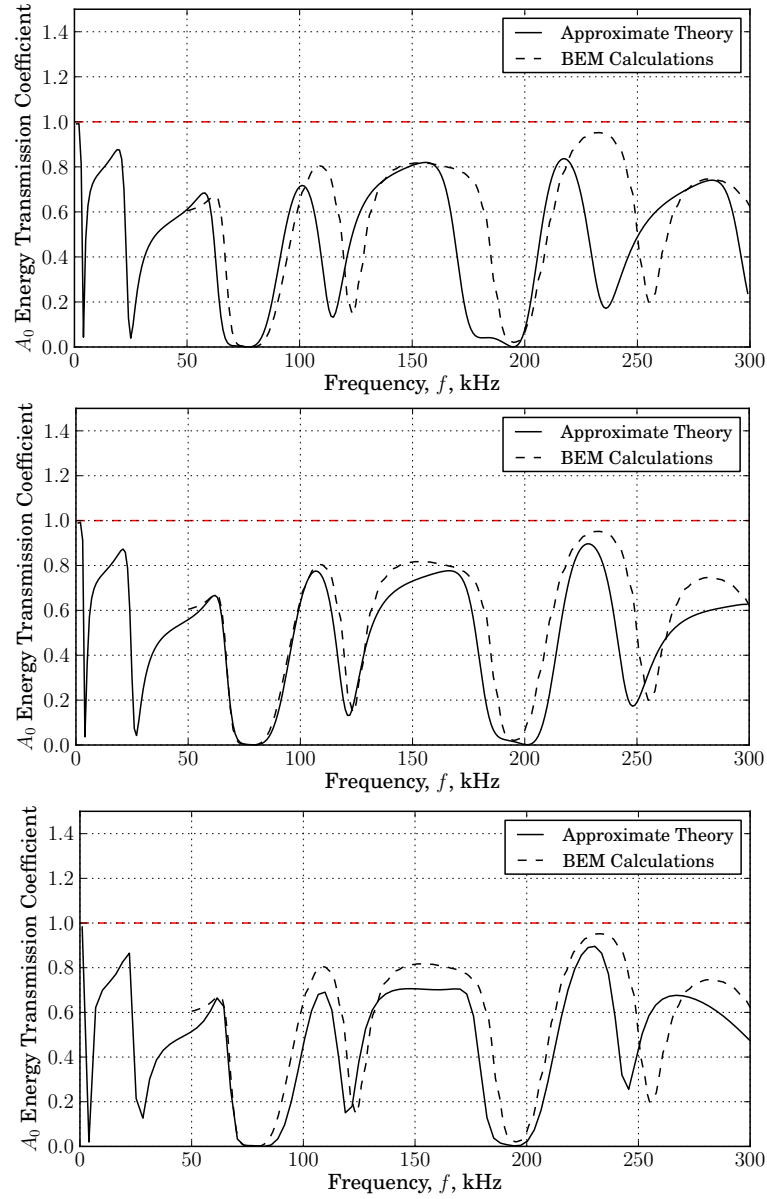
Figure A.1 A_0 Energy transmission coefficient for incoming A_0 waves using approximate theory without wavenumber correction (top), with wavenumber correction (middle), and with exact Lamb wave theory (bottom).